TRANSPARENT CONDUCTIVE OXIDE BI-LAYER AS FRONT CONTACT FOR MULTIJUNCTION THIN FILM SILICON PHOTOVOLTAIC CELLS

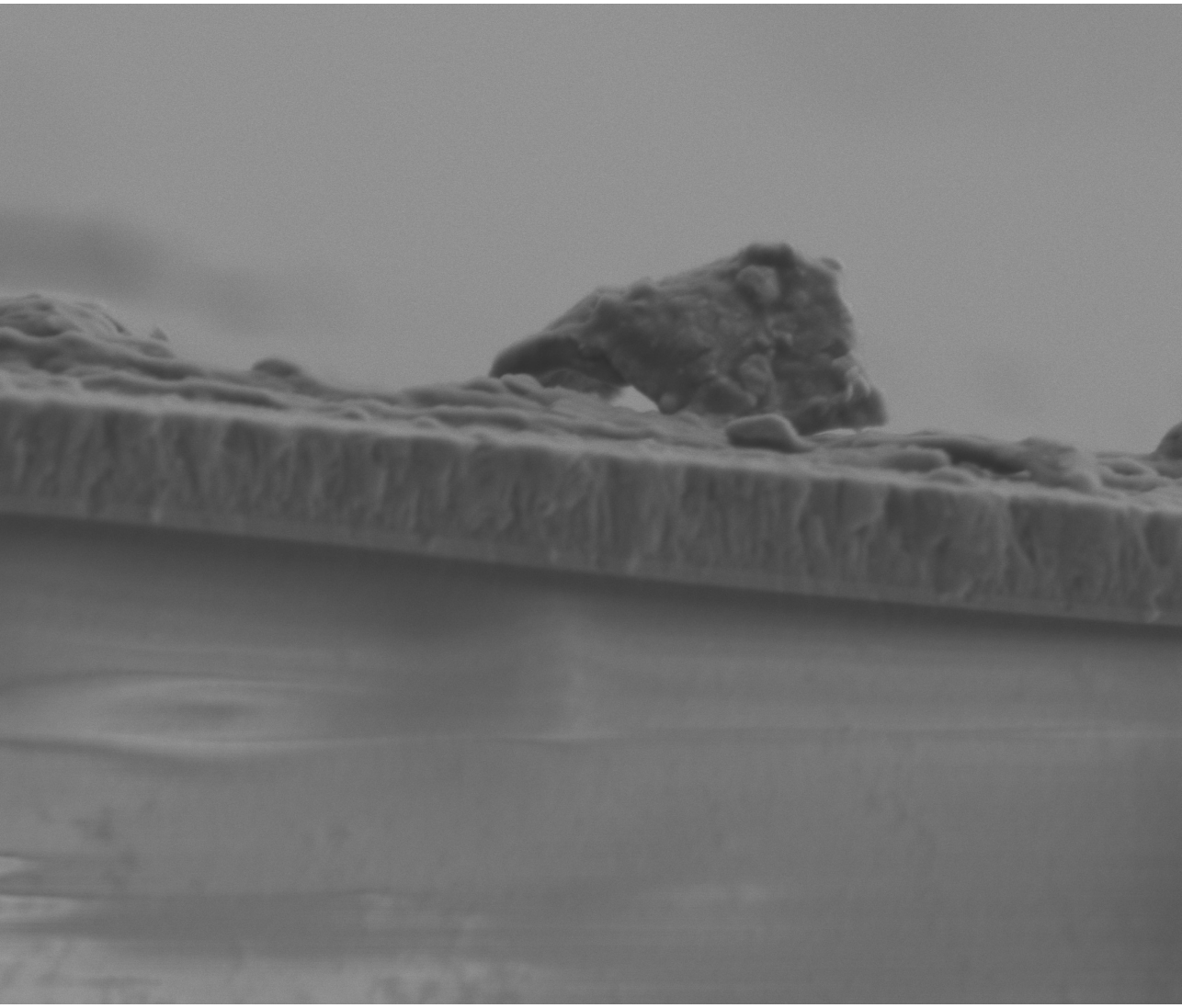

TRANSPARENT CONDUCTIVE OXIDE BI-LAYER AS FRONT CONTACT FOR MULTIJUNCTION THIN FILM SILICON PHOTOVOLTAIC CELLS

For the purpose of obtaining the degree of Master of Materials Science and Engineering

at Delft University of Technology,

to be defended publicly on March 27^{th} 2023

by

Prashand Kalpoe

Student number: 4385071

Composition of the thesis committee:

Dr. A. J. Böttger	Delft University of Technology, MSE
Prof. dr. ir. A.H.M. Smets	Delft University of Technology, PVMD
F. Saitta, MSc.	Delft University of Technology, PVMD

Supervisors:

F. Saitta, MSc.	Delft University of Technology, PVMD
Dr. G. Limodio	Delft University of Technology, PVMD
Prof. dr. ir. A.H.M Smets	Delft University of Technology, PVMD

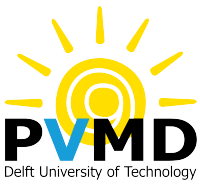

An electronic copy of this thesis is available at
https://repository.tudelft.nl/.

ABSTRACT

The journey towards increasing thin film solar cell efficiency is a continuously ongoing one, where each layer in the cell adds its own contributions and limitations. The transparent conductive oxide (TCO) is the first layer to encounter incident light on these cells and therefore needs to fulfil the requirement of high transparency. Carriers generated in the absorber layers of a thin film solar cell are transported to a metal electrode through the TCO, laying a conductivity requirement as well. A trade-off exists between transparency and conductivity, where one cannot be enhanced without sacrificing the other. Indium tin oxide (ITO) currently delivers the best trade off, thus is the most commonly applied TCO.

In this thesis study, candidate TCO materials were deposited and analysed in order to surpass the opto-electrical properties of ITO. In addition to depositing ITO, hydrogen doped indium oxide (IOH) and intrinsic zinc oxide (i-ZnO) thin films were deposited using RF magnetron sputtering. Substrate temperature, RF power, deposition time and H_2O partial pressure (only for IOH) were the varied parameters during depositions. IOH was found to surpass ITO in terms of conductivity, while i-ZnO surpassed ITO in terms of transparency. The best performing IOH and i-ZnO samples with regard to their respective superior parameters were chosen to be combined.

A TCO bi-layer was constructed by stacking a i-ZnO layer on top of a IOH layer. The IOH layer ensures good lateral conductivity, while the i-ZnO layer secures minimised parasitic absorption in the near infrared region. After being subjected to post deposition annealing, the bi-layer displayed opto-electrical properties superior to that of the individual i-ZnO and IOH layers. The highest electron mobility achieved for the bi-layer was 103,70 cm^2/Vs with a carrier density of $0,3*10^{20}$ $carriers/cm^3$. The working principle is the capping effect which i-ZnO has on IOH, keeping hydrogen contained within the bi-layer during annealing. Further investigation will lead to additional information on the behaviour of hydrogen within the as deposited bi-layer in comparison to the annealed one.

ACKNOWLEDGEMENTS

"A smooth sea never made a great sailor"
-The Red Heart Pump Pub

When I came to the Netherlands to start my BSc. in applied physics at the TU Delft in 2014, I had never imagined being able to achieve what I have. It has been a long and messy journey for me, but every event in my life has contributed to me being the person I am today. I look to the future with no regrets, only well taught lessons and aspire to continue developing myself as an engineer and as a person.

Dear Federica Saitta, if patience is a virtue, then you may be the most virtuous person I know, since your patience with me for the duration of this project has been astounding. You have never hesitated to share any of your knowledge with me and you were always ready to provide me with assistance. For this I am truly grateful and I am glad to have had you as my daily supervisor.

Prof. dr. ir. Arno Smets, Dr. Gianluca Limodio, Dr. Paula Perez Rodriguez and Govind Padmakumar. Your theories and willingness to help me have made this project as pleasant as possible. I am grateful to have had your support during my research and I hope to have contributed to even a fraction of yours.

Dr. Amarante Böttger, I would like to thank you for your guidance through the materials science aspect of my research. Your knowledge and suggestions have lead me to interesting findings which have contributed massively to my thesis.

To all my colleagues and friends at Roodhart Emission Control B.V., thank you for your understanding and leniency during my educational period. I would like to thank Dennis Bartens in particular. Dennis, you have provided me with the opportunity to keep developing myself career wise while simultaneously pursuing my masters degree. To me, you have been and will always be a true mentor and friend.

My close friends and family, you have been there for me and provided me with humour, strength, support and inspiration in difficult times. I would not know where to start if I were to return the favour. You have my heartfelt gratitude and I hope to someday be there for you as you have been for me.

Finally to my parents, both biological as well as "adoptive", you have provided me with unconditional love when I was not the easiest person to deal with. Your love, wisdom and support have been my guidance through troubling times in my life. I hope to have made you proud and yearn to someday be as wise and caring as you.

Prashand B. Kalpoe

CONTENTS

List of Figures

List of Tables

1

INTRODUCTION

Energy, the building block of modern society which has become an indispensable factor for mankind. The most prosperous and technologically developed countries are those which have access to as well as consume high amounts of energy. For decades, the energy crisis has been a well known problem with high importance around the world due to an increasing energy demand caused by a continuously growing population currently exceeding seven billion. Our present energy infrastructure is mainly based on fossil fuels (natural resources such as oil, coal and gas), which are depleted at a higher rate than they can be reproduced. Fossil fuels are burned in order to extract usable energy, which in turn produces so-called greenhouse gasses such as carbon dioxide (CO_2) and methane (CH_4) [1] [2].

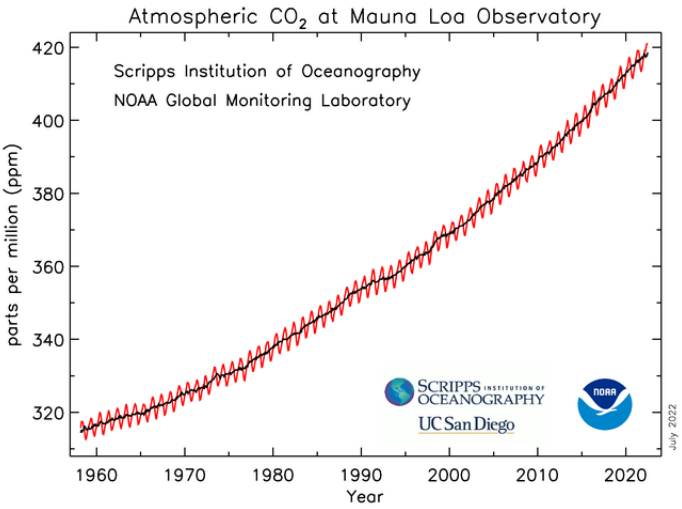

Figure 1.1: Atmospheric CO_2 measured at the Mauna Loa Observatory, Hawaii [3].

1

Figure 1.1 displays the strong increase in atmospheric carbon dioxide during the past sixty years observed at the Mauna Loa Observatory in Hawaii. Additional carbon dioxide produced by humans is stored either in the oceans or in the atmosphere, causing a global increase in temperature. In order to reduce carbon emissions, alternative means of harnessing energy from the sun, wind and water (hydroelectricity) are developed and utilised.

1.1. SOLAR ENERGY

Harnessing energy from the sun in order to produce electricity forms a very promising (partial) solution to the energy crisis. Devices with the ability to do so are called solar cells and need to be cost effective as well as reliable in order to compete with fossil fuels. Crystalline silicon (c-Si) makes up 90% of the photovoltaic (PV) market, thus dominates the PV scene due to its efficiency and well established manufactured c-Si cells. A major drawback of these cells is the cost of production (amount of material used), which in turn increases their payback time. As a means of increasing efficiency, cells are deposited on wafers. Even so, high amounts of expensive material usage is solved with an alternative solution, the so called thin film cell technology. Thin film cells are the second generation of solar cells, which if optimised have the potential to commercially surpass traditional wafer based solar cells. Active absorber layers present in these cells are in the order of nanometers to micrometers, producing lightweight devices. Figure 1.2 illustrates three commercialised direct bandgap thin film solar cells: amorphous silicon (α-Si), copper indium gallium selenide (CIGS or CIS excluding gallium) and cadmium telluride (CdTe) cells.

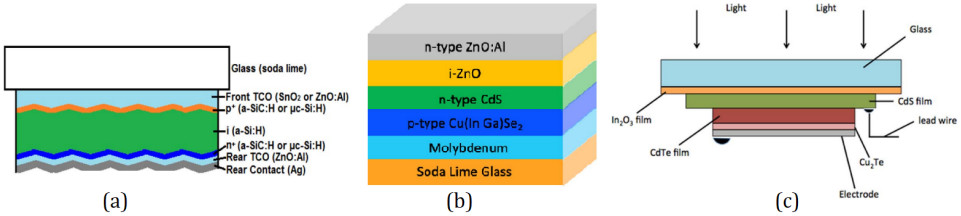

Figure 1.2: Schematic representation of (a). Amorphous silicon (α-Si) solar cell; (b). Copper indium gallium selenide (CIGS or CIS excluding gallium); (c). Cadmium telluride (CdTe) [4].

Efficiency's of 13,6% were achieved for laboratory α-Si cells, which is significantly lower than the 22,8% efficiency of a traditional consumer wafer based solar cell. Laboratory CdTe and CIS cells have been reported to have achieved efficiency's of 22,1% and 22,9% respectively [4] [5]. These efficiency's are close to or even surpass those of a traditional solar cell, proving that thin film cells have the potential to supersede traditional cells. In the solar cell structures illustrated in figure 1.2, an interesting similarity between the three is the presence of one or more transparent

conductive oxide (TCO) layers. TCO's are optically transparent and electrically conductive thin film materials applied in touch panels, liquid crystal displays (LCD's), organic light emitting diodes (OLED's) etc. In each application, the applied TCO may be modified in order to meet specified requirements. For PV application, TCO's are used as front and back electrodes as well as a back reflector. As a front electrode, the TCO should have a high transparency (reflection and absorption of light should be minimal) in order to let a significant amount of light pass through to reach the (often silicon) absorber layers in the cell. A back contact TCO needs to be highly reflective in such a way to allow light to pass through the cell again. In both cases, conductivity should be high in order to transport carriers generated when light interacts with the absorber layers. For the purpose of minimising electrical losses, a minimised lateral resistance is also necessary.

1.2. RESEARCH MOTIVATION

This thesis project is part of the research towards a high performance PV cell architecture based on thin-film hydrogenated amorphous silicon/nanocrystalline silicon tandem cells. The objective of the front window/contact layer or TCO of this devices is to realise i) a high lateral conductivity in combination with ii) a low infrared absorption in order to realise maximum current generation in the bottom cell. Currently, the indium tin oxide (ITO) window layer has the best performance with respect to i) and ii) or in other words has the most beneficial compromise between free charge carrier absorption and conductivity. In this project, the goal is to surpass the performance of ITO by the introduction of a window layer based on a double layer (hereafter referred to as bi-layer) of two different TCO's. One TCO material will be optimised for conductivity, while the other TCO will be optimised for transparency and absorption in the infrared.

In order to find a suitable substitute for ITO, a number of different TCO's as listed below will be deposited using RF magnetron sputtering.

TCO's to be deposited using RF sputtering:

- Indium tin oxide (ITO) as reference
- Hydrogen doped indium oxide (IOH)
- Intrinsic zinc oxide (i-ZnO)

Previous works have singled out IOH as the TCO with highest achievable conductivity (higher than ITO). This will be investigated by characterising and comparing the previously mentioned TCO's, after which the possibility of producing a TCO double layer consisting of IOH and the TCO with the lowest absorbance will be explored. It is proposed to use IOH for its superior conductivity and i-ZnO for its superior transparency and low infrared absorption.

Main research question:
Can a TCO bi-layer be constructed which outperforms the electrical and optical

properties of ITO by minimising structural losses?

Sub-questions:

- What processing conditions influence the electrical and optical properties of IOH and i-ZnO and in which way do they influence these properties? What are the best electrical and optical properties that can be obtained? What are the limiting mechanisms?
- What are the design principles of the bi-layer to achieve the highest optical and electrical functionality?

2

THEORY

2.1. OPTICS

Before explaining the theory behind PV cells, a basic understanding of the optics at play is required, which will be provided in the current section. Electromagnetic waves transversing between two non-absorptive media media are partly reflected where the angle of reflected light is equal to the incident angle. The non-reflected part, will enter the second medium and will be refracted.

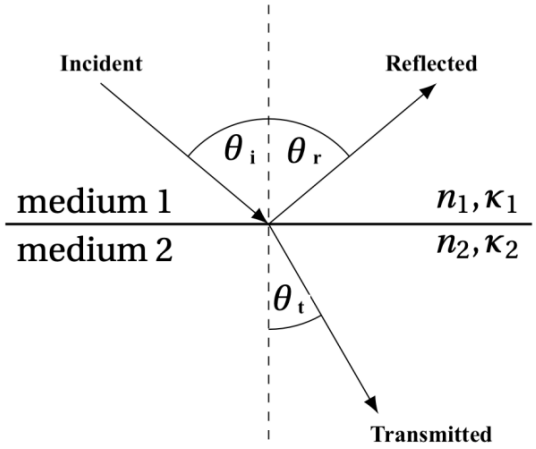

Figure 2.1: Paths of an incoming ray of light travelling from one medium (n_1) to another (n_2). A portion of the incoming light is reflected back to the first medium, while the other part is refracted, travelling in the second medium [6].

The angle of refracted light θ_t is related to the angle of incident light θ_i through Snell's law.

$$n_1 \cdot sin\theta_i = n_2 \cdot sin\theta_t \tag{2.1}$$

Where it is important to remember that both media are assumed to be non-absorptive, thus only the real parts of the respective refractive indices n_1 and n_2 are considered. Relations between the magnitudes of the incident, reflected and refracted light are given by Fresnel's equations. A distinction is made between parallel (equations (2.2)) and perpendicular (equations (2.3)) polarized light.

$$T_\parallel = \frac{2 \cdot n_1 \cdot cos\theta_i}{n_1 \cdot cos\theta_t + n_2 \cdot cos\theta_i}, R_\parallel = \frac{n_1 \cdot cos\theta_t - n_2 \cdot cos\theta_i}{n_1 \cdot cos\theta_t + n_2 \cdot cos\theta_i} \tag{2.2}$$

$$T_\perp = \frac{2 \cdot n_1 \cdot cos\theta_i}{n_1 \cdot cos\theta_i + n_2 \cdot cos\theta_t}, R_\perp = \frac{n_1 \cdot cos\theta_i - n_2 \cdot cos\theta_t}{n_1 \cdot cos\theta_i + n_2 \cdot cos\theta_t} \tag{2.3}$$

For non-polarized light, the mean of the two squared polarizations is used in order to obtain the reflectivity and transmittance. These equations provide accurate relations for light travelling between two non-absorptive media, however when applying these equations for absorptive media, it is important to note that the they provide a mere approximation. For an absorptive material, its complex refractive index consists of the sum of a real and an imaginary part.

$$\tilde{n} = n + i\kappa \tag{2.4}$$

The real part n is used for non-absorptive media and the imaginary part κ known as the extinction coefficient, is characterised by equation (2.5).

$$\kappa = \frac{\alpha\lambda}{4\pi} \tag{2.5}$$

Where α is the absorption coefficient and λ the wavelength in vacuum. For absorptive media, the refractive index in equations 2.2 and 2.3 is to be replaced with the complex refractive index [1] [5].

2.2. SOLAR CELL OPERATING PRINCIPLE

The working principle of solar cells is based on the photovoltaic effect i.e. the generation of a potential difference at the junction of two different materials when exposed to electromagnetic radiation. This is closely related to the photoelectric effect, where a material absorbs light in order to emit electrons. Photons are a defined energy quanta of light possessing energy as described by equation (2.6).

$$E = h\nu = \frac{hc}{\lambda} \tag{2.6}$$

Where h stands for Planck's constant (6,63 * 10^{-34}m^{2}kg/s) and v for the frequency of light which is defined as the speed of light (c $\approx$ 3*10^8 m/s) divided by its wavelength λ. When a semiconductor is exposed to light, an electron may absorb the light's contained photon energy and may be excited from the valence band (lower state of energy) to the conduction band (higher state of energy) provided the incoming photon contains enough energy in order to satisfy the following condition.

$$hv = E_f - E_i \tag{2.7}$$

In equation 2.7, E_f is the higher energy level and E_i the initial one. When an electron is excited to a higher energy state, it leaves behind a void in the form of a positively charged elementary particle called a hole.

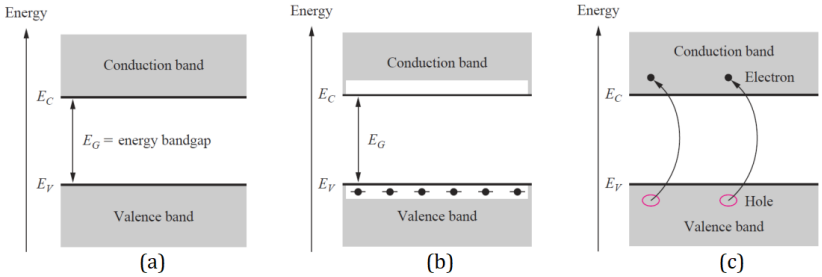

Figure 2.2: (a). Energy band model for a semiconductor with bandgap E_G; (b). Semiconductor at 0 K with filled valence band and empty conduction band; (c). Electron-hole pair generation by thermal excitation across energy bandgap [7].

Figure 2.2 describes the generation of a electron-hole pair when a photon is absorbed by a semiconductor. The energy difference between the bottom of the conduction band and top of the valence bad is called the bandgap energy E_G [1].

2.3. SEMICONDUCTORS

Semiconductor materials have (influenceable) electrical conductivity between that of a conductor and an insulator. The first working solar cell was constructed using the still widely applied crystalline silicon, which will be used in this section in order to explain the working principle of semiconductors. Silicon has four valence electrons which can form chemical bonds with other atoms. Two Si atoms are covalently bonded when they share each other's valence electrons, meaning that each Si atom can be bonded to four other Si atoms. When the atomic structure of Si contains a low concentration of foreign (impurity) atoms, it is categorised as an intrinsic semiconductor. At 0 K, all valence electrons form bonds with neighbouring Si atoms as seen in figure 2.3. At temperatures higher than 0 K however, a breakage of covalent bonds between Si atoms occurs due to the absorption of thermal energy.

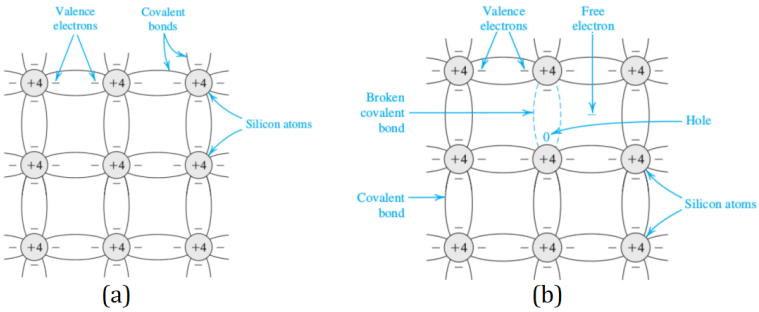

Figure 2.3: (a). Silicon crystal lattice at 0 K, where all covalent bonds are intact; (b). Silicon crystal lattice at room temperature, where some covalent bonds are broken, resulting in electron-hole pairs [7].

When a bond between two Si atoms is broken, the valence electron shared by these two atoms is liberated and can move freely throughout the crystal lattice. Liberation of this free electron also results in creation of a positively charged particle left behind by the electron called a hole. Valence electrons from neighbouring atoms may be released from their initial position in order to fill the hole restoring the initial broken bond, resulting in the creation of another hole. This recurring event visualises the movement of the hole throughout the lattice in the opposite direction of the valence electron. For intrinsic semiconductors, the breakage of covalent bonds leads to electron-hole creation, which means that the amount of broken bonds is equal to the concentration of electrons as well as the concentration of holes noted as the intrinsic carrier concentration. For intrinsic silicon at 300 K, approximately $1,5 * 10^{10} \text{cm}^{-3}$ broken bonds (equal to the electron and hole concentrations) are present. Intrinsic semiconductors are favourable when one wishes to have low levels of impurities in the lattice. One of the advantages of semiconductors however, is the susceptibility to the introduction of impurities to the crystal lattice as a means of influencing electron or hole concentrations. The process of replacing silicon atoms in a way that influences the carrier concentration is called doping and changes the categorisation of the semiconductor from an intrinsic into an extrinsic one. A doped semiconductor can either be an n-type or p-type semiconductor depending on whether electrons or holes respectively dominate the electrical conductivity.

- Negatively doped (n-type) semiconductors are doped with atoms containing an extra valence electron compared to the original atom they replace. For c-Si, group V elements such as phosphorous, arsenic, antimony and bismuth are used in order to turn it into an n-type semiconductor. When a silicon atom is replaced with a group V atom, only four out of five valence electrons of the group V atom are bonded to four silicon valence electrons. The fifth electron is weakly bound to the group V atom core and can be released at room temperature due to the absorption of thermal energy by the silicon lattice as illustrated in figure 2.4a. These atoms are called donors, because they donate

free electrons to the c-Si lattice.

- Positively doped (p-type) semiconductors are doped with atoms containing one valence electron less than the original atom they replace. Group III elements such as (mainly) boron, aluminium, gallium and indium are used for turning c-Si into a p-type semiconductor. Group III atoms cannot form bonds with all four neighbouring silicon atoms, because they only have three valence electrons. At room temperature, an adjacent silicon atom releases an electron which attaches itself to the group III atom in order to bond it to all four neighbouring silicon atoms as illustrated in figure 2.4b. This event leads to the a negatively charged group III atom, but the electron released for this process leaves behind a hole at the adjacent silicon atom. For this reason, group III atoms are called acceptors, because they introduce holes into the silicon lattice which can readily accept electrons.

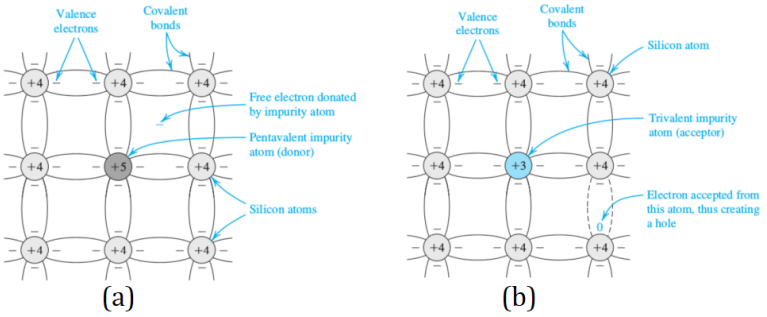

Figure 2.4: (a). Silicon doped with column V impurity. As a result, a free (donated) electron is able to move around the lattice; (b). Silicon doped with column III impurity. An extra unfilled bond results in a hole which can accept electrons in the lattice [7].

Introduction of donors and acceptors into the lattice allows the existence of energy levels between the conduction and valence bands. Valence electrons (weakly) bound to a donor atom occupy energy levels close to the conduction band indicating that the electron is localised in the vicinity of the donor atom. In a similar way for acceptors, holes occupy energy levels close to the valence band. The Fermi energy or Fermi level, defined as the highest occupied energy level by valence electrons and lies between the conduction and valence bands for intrinsic semiconductors, is also influenced by doping. In a n-type semiconductor, the Fermi level will shift closer to the conduction band depending on the donor concentration. When a semiconductor is p-doped, the Fermi level will shift closer to the valence band depending on the concentration of acceptors [1] [5].

2.3.1. BANDGAP

Taking a look into the bandgap of semiconductors, a distinction can be made between direct and indirect bandgap semiconductors. The difference between the

two is explained using the dispersion diagrams shown in figure 2.5.

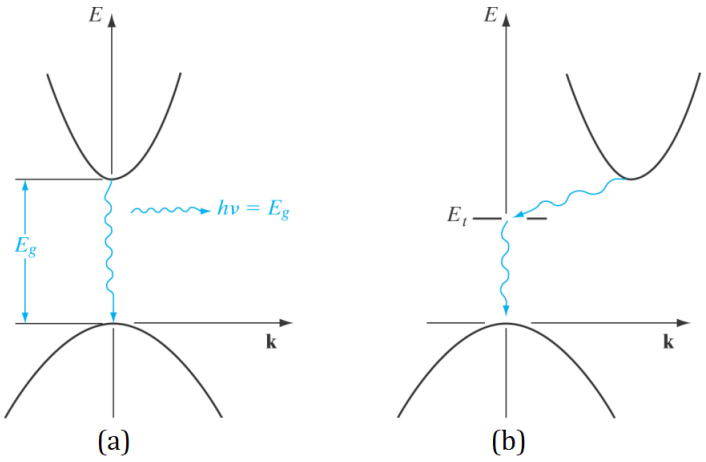

Figure 2.5: (a). Direct bandgap semiconductor. Maximum of the valence band is aligned with the minimum of the conduction band; (b). Indirect bandgap semiconductor. Maximum of the valence band is not aligned with the minimum of the conduction band [7].

In figure 2.5, the vertical axis is represented by the energy state and the horizontal axis by the charge carrier momentum. Figure 2.5a shows a direct bandgap material, which means that the maximum of the valence band and minimum of the conduction band are aligned with each other. In this case, for an electron to be excited from the valence band to the conduction band, it only requires the energy provided by absorbing a photon. When a semiconductor has an indirect bandgap (such as c-Si) as illustrated in figure 2.5b where the maximum and minimum of the valence and conduction bands respectively are not aligned, an electron requires energy (vertical) as well as momentum transfer (horizontal) in order to be excited to the conduction band. The energy is still provided by absorbed photons, but the momentum transfer is required to be provided by vibrations of the crystal lattice. Comparable to photons, these crystal lattice vibrations can be described as waves as well as particles and are defined as phonons. An electron acquires a change in momentum when it absorbs a phonon from the crystal lattice [1]. One can imagine that electron excitation from valence band to conduction band is easier for a direct bandgap material, which due to this reason has a higher absorption coefficient compared to an indirect bandgap material.

2.3.2. RECOMBINATION MECHANISMS

DIRECT RECOMBINATION

Generation and recombination processes that happen from bandgap to bandgap are called direct generation and recombination and are more likely to happen in direct

badgap materials, because no change in momentum is required for exciting an electron from the valence band to the conduction band. These processes are usually radiative meaning that an electron-hole pair is created upon photon absorption, vice versa a photon is emitted if electron-hole pairs recombine directly.

SHOCKLEY-READ-HALL RECOMBINATION

For Shockely-Read-Hall (SRH) recombination, electrons and holes do not recombine directly from bandgap to bandgap instead, the recombination is facilitated by impurity atoms and lattice defects. These impurity atoms and lattice defects are usually present in smaller concentrations compared to donor and acceptors and allow energy levels within the bandgap acting as trap states. SRH recombination is non-radiative and is the dominant recombination mechanism in semiconductors at most operational conditions. Excess energy generated during the process is dissipated into the lattice in the form of heat. A distinction can be made between donor traps and electron traps. Donor traps are neutral when they contain an electron and have a positive charge when they do not, while acceptor traps are negatively charged when they contain an electron and neutral when they do not. A single electron trap consists of the following processes in order of listing.

- Electron capture from conduction band;
- Electron emission to conduction band;
- Hole capture from valence band;
- Hole emission to valence band.

Electron and hole capture rates are proportional to the free carrier concentration, thermal velocity, trap density and trap occupancy by electrons or holes. The emission rates are proportional to the trap density and the electron or hole occupancy of the traps, as well as the emission coefficient for electrons or holes.

AUGER RECOMBINATION

Auger recombination is a process occurring in indirect semiconductors involving three particles. The momentum and energy of recombining an electron and a hole is conserved by transferring it to another hole (or electron) If the energy is transferred to an electron, it is excited to higher energy levels within the conduction band. When this excited electron relaxes, it transfers its energy to vibrational energy of the lattice (phonon modes) and finally into heat. If the third particle is a hole, a similar process occurs, except that the hole is excited to deeper levels of the valence band. The recombination rate is strongly dependent on the electron and hole charge carrier densities.

SURFACE RECOMBINATION

At the surface of a material, many valence electrons cannot form a covalent bond resulting in defects called dangling bonds. These dangling bonds introduce surface trap states within the bandgap resulting in SRH recombination. Surface recombination may be the dominant mechanism in very pure semiconductors.

2.3.3. JUNCTIONS

Most solar cells consist of a junction between oppositely doped semiconductors. A junction between a p-type semiconductor and an n-type semiconductor of the same base material is called a p-n homojunction, while a p-n heterojunction is one consisting of different materials. When a p-type and n-type -semiconductor are joined, the large difference in carrier concentration between the two causes holes to diffuse from the p-type semiconductor to the n-type semiconductor, while electrons from the n-type semiconductor diffuse to the p-type semiconductor. The diffusion process depletes the area close to the metallurgical junction of mobile charge carriers, which eventually grows into a space charge created by the ionized donor and acceptor atoms. Charge neutrality is conserved in the quasi-neutral regions outside this depletion region as depicted in figure 2.6.

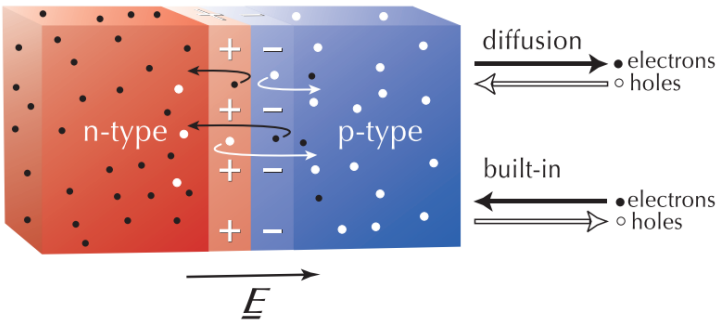

Figure 2.6: Diffusion of electrons and holes when a n-type and p-type semiconductor make contact with each other. A depletion region is clearly observed when the amount of electrons present in the n-type semiconductor along with the amount of holes present in the p-type semiconductor are compared to the area around the metallurgical junction [8].

Figure 2.6 also shows the generation of an electric field due to the presence of positive and negative ions in the area around the junction. This electric field causes charge carriers to move in the opposite direction of their respective concentration gradients. Charge carriers continue to diffuse across the junction until the diffusion force acting on the carriers and the drift force caused by the electric field cancel each other out. The p-n junction will then be in equilibrium. Figure 2.7a and figure 2.7b represents the band diagram of individual p-type and n-type semiconductors respectively. Figure 2.7c shows the band diagram when the two are connected.

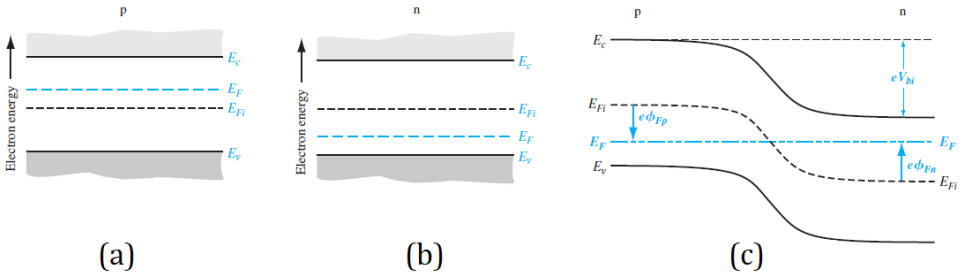

Figure 2.7: (a). Band diagram of p-type and p-type semiconductor; (b). Band diagram of p-type and p-type semiconductor; (c). Band diagram of p-n-junction [9].

As one can notice, the individual semiconductors also have their independent Fermi levels (close to the valence band for a p-type material and close to the conduction band for an n-type material), but when the two are connected and the junction reaches equilibrium, the Fermi level is constant across the junction as illustrated by figure 2.7c. When connected, the band edge energies E_C and E_V as well as the vacuum energy must be continuous, which leads to band bending. The bands are bent due to the presence of an electric field, which causes a difference in electrostatic potential between the boundaries of the depletion zone. Changes in the electrostatic potential compensate changes in carrier concentration in this zone.

Another important type of junction in solar cells aside from semiconductor junctions are metal-semiconductor junctions. Metals (conductors) are often used as back as well as front contacts in order to connect the solar cell to an external circuit. Figure 2.8a shows the individual band diagram of a metal and an n-type semiconductor.

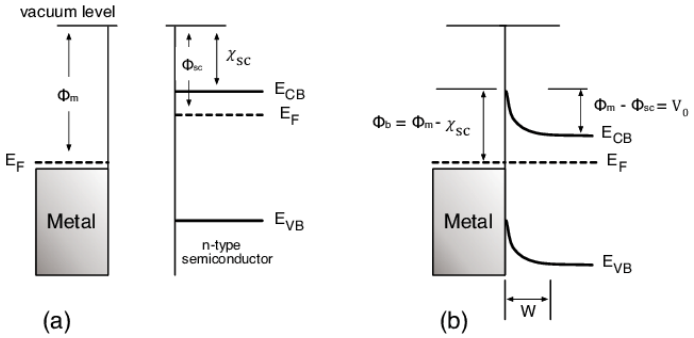

Figure 2.8: (a) Band diagram of individual metal and n-type semiconductor. (b). Band diagram of metal-semiconductor junction [10].

For an ideal metal-semiconductor contact, the Fermi level and the vacuum level must be constant at thermal equilibrium, which results in the formation of a barrier between the two as illustrated in figure 2.8b. When a positive external voltage is applied to the junction, the barrier height for an electron to travel from the n-type semiconductor to the metal decreases. Applying a negative external voltage increases the barrier, making it more difficult for electrons to be transferred to the metal. This also applies for a p-type semiconductor, except for opposite voltage polarizations [1].

2.4. TRANSPARENT CONDUCTIVE OXIDES (TCO)

Several materials such as metal oxides, metal nanowires, carbon nanotubes (CNTs), organic semiconductors, and 2D materials such as graphene and molybdenum disulfide (MoS_2) have been developed for transparent electrode application in optoelectrical devices. Metal oxides are conventional and competitive contenders to use as materials for TCO due to the combination of high optical transparency, good electrical properties, straightforward synthetic access, large-area electrical uniformity and mechanical flexibility. The quality of opto-electrical properties in metal oxides depends strongly on the number of impurities (intentionally) incorporated into the film. An important parameter to consider for TCO in photovoltaic application is the lateral conductivity described by equation (2.8).

$$\sigma = N \cdot e \cdot \mu = \frac{1}{\rho} \tag{2.8}$$

Conductivity (σ) is a product of carrier concentration (N), elementary charge (e) and mobility (μ). The resistivity (ρ) is obtained when taking the inverse of conductivity and vice versa. With the elementary charge being a constant, high carrier concentration and mobility are required in order to achieve high conductivity. Carrier concentration can be increased by a higher amount of doping during deposition, this however deteriorates the optical transparency, which is undesirable for pv applications. Thus high mobility and moderate carrier concentration are crucial factors in TCO with good opto-electrical properties [11][12].

2.4.1. SCATTERING MECHANISMS

Carrier transport in semiconductors is described by electronic structures in the reciprocal space, where electron and hole effective masses are determined by the respective CBM and VBM curvatures. The electron effective mass is a measure of the mass an electron seems to have when moving through a periodic solid, while the mobility indicates how fast an electron can move through the solid in the presence of an electric field. The two are related as depicted by equation (2.9).

$$\mu = \frac{e \cdot \tau}{m_e^*} \tag{2.9}$$

Where τ is the carrier relaxation time which is determined by a number of scattering mechanisms in the material. The total relaxation time is a superposition of individual contributions.

$$\frac{1}{\tau_{total}} = \frac{1}{\tau_{phonon}} + \frac{1}{\tau_{cc}} + \frac{1}{\tau_{GB}} \tag{2.10}$$

The terms present equation 2.10 are relaxation times from optical phonon scattering (τ_{phonon}), charged center (ionized impurity) scattering (τ_{cc}) and grain boundary scattering (τ_{GB}). Scattering from dislocations, acoustic phonons and neutral impurities are assumed to be negligible. Seeing as the mobility is a function of relaxation time, it can also be considered to be a sum of similar individual elements.

$$\frac{1}{\mu_{total}} = \frac{1}{\mu_{phonon}} + \frac{1}{\mu_{cc}} + \frac{1}{\mu_{GB}} \tag{2.11}$$

Many efforts have been made in order to increase conductivity by increasing the carrier concentration in a TCO. In spite of the increase in conductivity, this method is self limiting in the sense that it introduces many dopant sites which reduce the relaxation time due to dopant (impurity) scattering. The major consequence of this event is a reduction in mobility, thus obtaining the highest possible conductivity is a trade off between carrier concentration and mobility [11].

PHONON SCATTERING

Phonons in single as well as polycrystalline materials are defined as interactions with vibrational modes of the crystal lattice. At temperatures higher than 0 K, charge carriers may be scattered by generated phonons. The mobility due to this type of scattering can be estimated from temperature dependent mobility values [11][12].

CHARGED CENTER (IONIZED IMPURITY) SCATTERING

Charged center (ionized impurity) scattering is an important factor to consider for TCO doped with oxygen vacancies and/or impurity atoms. At locations in a crystalline structure where electrons become freely mobile, an ionized impurity is left behind, which is able to scatter charge carriers. This form of scattering is the dominant scattering mechanism in a doped material. High carrier concentrations make it difficult to predict μ_{cc}, due to impurity clustering [11][12].

GRAIN BOUNDARY SCATTERING

Grain boundary's can be visualised as the interface between two grains in polycrystalline materials, which are prone to act as defect sources leading to

deterioration of material properties. These defects may operate as carrier traps, creating potential barriers which can hinder inter grain carrier transport [11][12].

2.4.2. OPTO-ELECTRICAL TRADE OFF

Fabricating an optimal TCO not only relies on the electrical limitation, due to the relationship between the electrical and optical properties where one often needs to be sacrificed in order to enhance the other. Irradiation by light in the ultra violet wavelength range leads to optical absorption leading to inter band transitions between the valence and conduction band. The optical band gap in degenerate TCO is broadened by the Moss-Burnstein shift, which is beneficial for PV applications since a broader range of wavelengths is utilised. The presence of lattice defects such as oxygen vacancies, proton interstitials and substitutional defects (in an n-type TCO) result in a surplus of electrons near the defect site. Delocalisation of the electrons from the defect sites is permitted when there is sufficient orbital overlap resulting in filled conduction band minimum states causing a shift in Fermi level above the CBM. This leads to the well known Moss-Burnstein effect (or Moss-Burnstein shift) which effectively widens the optical bandgap. At wavelengths in the near infrared region (NIR), optical absorption occurs due to intra-band transitions in the conduction band well known as free carrier absorption (FCA). In metals and semiconductors, the FCA is modelled by a Drude oscillator where the absorption coefficient (α_{FCA}) is described as follows.

$$\alpha_{FCA} = \frac{\lambda^2 e^3 N}{4\pi^2 \epsilon_0 c^3 n (m_e^*)^2 \mu_{opt}} \tag{2.12}$$

In equation 2.12, λ is the photon wavelength, e the elementary charge, N is the free carrier concentration, ϵ_0 the permittivity in vacuum, n is the refractive index, m_e^* the effective electron mass and μ_{opt} the optical mobility. Equation (2.12) shows the direct proportionality between the absorption coefficient, wavelength and carrier concentration. When a conductor is irradiated with electromagnetic waves, the carriers of that conductor oscillate with the same frequency as these waves (plasma oscillation). The threshold frequency for plasma oscillation is characterised by the plasma frequency ω_p.

$$\omega_p^2 = \frac{Ne^2}{\epsilon_0 \epsilon_\infty m_e^*} \tag{2.13}$$

Where N is the density of free charge carriers, e the elementary charge, ϵ_0 and ϵ_∞ the vacuum and high- frequency permittivity respectively and m_e^* is the effective electron mass. When a conductor is exposed to light with a frequency higher than its plasma frequency, its carriers cannot catch up with the quick electric oscillation, resulting in light being transmitted through the conductor without triggering plasma oscillation or surface reflection. Instead of the plasma frequency, the threshold

for plasma oscillation can also be described using plasma wavelength described by equation 2.14.

$$\lambda_p = \frac{2\pi c}{e}\sqrt{\frac{\epsilon_0 m_e^*}{N}} \tag{2.14}$$

Photons with wavelengths larger than λ_p (wavelength corresponding to plasma frequency), are reflected by the TCO [11]. A general TCO transmission spectrum is illustrated in figure 2.9.

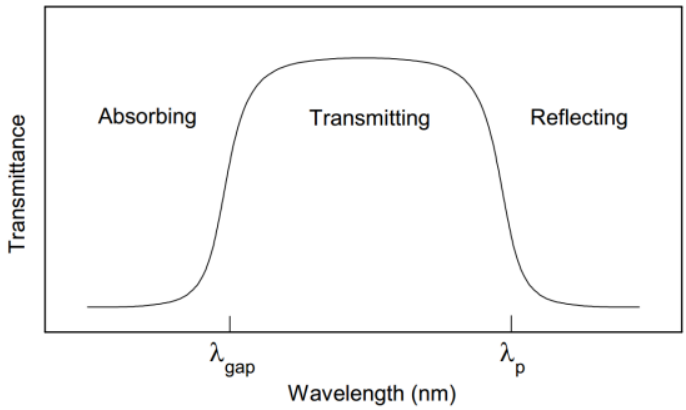

Figure 2.9: General transmission spectrum of a TCO. λ_{gap} corresponds to the wavelength below which bandgap absorption takes place. λ_p corresponds to the wavelength beyond which plasma oscillation occurs [12].

Incoming photons with a wavelength lower than λ_{gap} (wavelength corresponding to the bandgap) get absorbed due to the photon containing more than enough energy in order to surpass the bandgap, leading transitions from the valence to the conduction band.

DEPOSITION CONFIGURATIONS

Two general configurations for depositing solar cell layers exist: the superstrate and substrate configurations. The main difference between the two is the order in which layers are deposited, which in turn provides different layer properties depending on the materials, deposition methods -and conditions.

SUPERSTRATE CONFIGURATION (P-I-N CONFIGURATION)

Figure 2.10(a) illustrates the superstrate configuration for depositing solar cells. Glass is usually used as superstrate in this configuration due to its high transparency and ability to handle the chemical and physical deposition conditions for the different

layers. The TCO is deposited on the glass first followed by a p-layer (order of 10 nm thick). After the p- layer, comes an intrinsic layer which usually is a few hundred nanometers thick where absorption takes place. The n-layer (around 20 nm thick) is deposited on top of the intrinsic layer. Finally, the back contact is deposited which is configured by a thin TCO and thick metallic layer for reflecting unabsorbed light back to the intrinsic layer [1] [5].

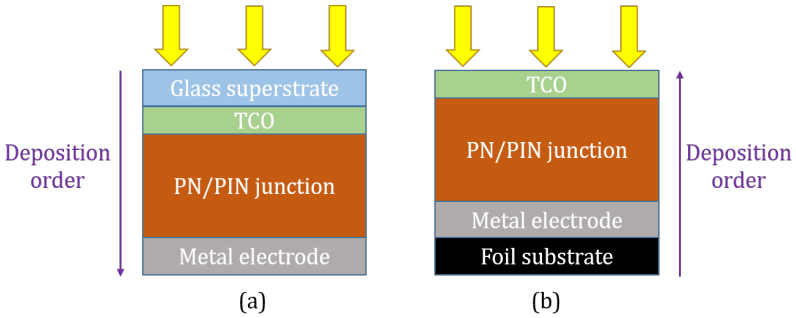

Figure 2.10: (a). Simplified depiction of a superstrate configuration, where the TCO is deposited on top of a glass superstrate followed by a p-n/p-i-n junction and finally a metal electrode. (b). Simplified depiction of a substrate configuration where a metal electrode is deposited on top of a substrate followed by a p-n/p-i-n junction and finally a TCO.

SUBSTRATE CONFIGURATION (N-I-P CONFIGURATION)

An alternate configuration is the substrate or n-i-p configuration illustrated in figure 2.10b where either the substrate acts as a back contact or a back contact is deposited on top off the substrate. In this configuration, light first encounters the layer deposited last (the TCO) and no light passes through the substrate. In general, polymers are some of the materials used for substrates. The n-layer is deposited first on top of the substrate or metal electrode followed by an intrinsic layer, a p-layer and finally the TCO.

3

Deposition and Characterisation

3.1. Method

This section will provide an overview of the deposition equipment and method along with equipment used for characterisation. Corning glass substrates of 10x2,5 cm were cleaned in an ultrasone bath in acetone followed by isopropanol for a total of 20 minutes, after which they were either air dried or blow dried with nitrogen gas. TCO films were deposited on these cleaned substrates using RF magnetron sputtering in the available sputtering equipment. Deposition properties were varied in order to investigate the effects of deposition conditions on the opto-electrical properties of the TCO. The following properties were varied depending on the deposited TCO: substrate temperature, RF power, deposition time and H_2O partial pressure. Deposition recipes were created in order to demonstrate the influence of these individual parameters on the optical and electrical properties of the deposited TCO films and provide parameters for obtaining films of a desired quality. The following targets were sputtered in order to create their respective TCO films.

- Indium tin oxide containing 3% tin for ITO;
- Stochiometric indium oxide for IOH and
- Stochiometric zinc oxide for i-ZnO

3.2. Magnetron Sputtering

Magnetron sputtering is a form of physical vapour deposition used to deposit thin films on a substrate by bombarding the target source material with plasma or gas particles. This technique has the advantages of simple equipment, easy control, large coating area and strong adhesion.

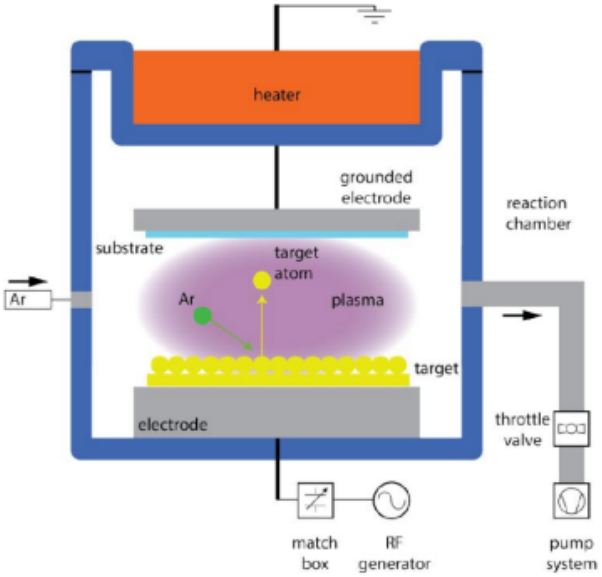

Figure 3.1: Working principle of the sputtering process [13].

The process takes place in a vacuum chamber where a plasma glow discharge is applied between two parallel plates, the substrate (anode) and the sputtering target (cathode). The process chamber is pumped to vacuum followed by the introduction of an inert gas (usually argon) which does not react with the target material or other process gasses. Argon atoms have a high molecular weight resulting in an increased sputtering yield and high deposition rate. The plasma glow discharge ignited by applying a DC or RF (AC) bias depending on the target material. A DC bias is commonly used in the case of conductive materials, preventing the accumulation of electric charge, while an RF bias may be applied for both conductive and non-conductive materials. Argon ions gain energy and momentum through collisions within the plasma. Magnetron sputtering increases the plasma density by introducing a magnetic field to the surface of the target cathode and utilising the constraints of the magnetic field on the charged particles to increase the sputtering rate. The positively charged argon ions then collide with the target surface resulting in ejection of atoms from the target material, which diffuse from cathode (target) to anode (substrate) eventually forming a thin film. Films with better uniformity, homogeneity, less trap densities and high carrier mobility were reported to have been achieved using RF sputtering. Both DC and RF sputtering could induce damage to the substrate surface during the deposition process. The damage from DC sputtering is known be caused by particle bombardment, while ultraviolet radiation emission resulted in substrate/film damage during RF sputtering. [14].

During sputtering, atoms released from the target condensate on to the substrate resulting in bonded adatoms, which diffuse over the surface until they desorb,

or more likely are trapped at low energy lattice sites. These atoms reach their final equilibrium positions through bulk diffusion. A distinction can be made between four processes: shadowing, surface diffusion, bulk diffusion and desorption, where the last three are quantified by characteristic diffusion and sublimation activation energies whose magnitudes scale directly with the melting point of the condensate. Shadowing is a result of the geometric constraint imposed by the growing film's roughness and the line-of-sight impingement of arriving atoms. Substrate temperature (T_s) determines the ruling process resulting in different structural morphologies. A general relation between sputtering parameters and the microstructure of sputtered metal thin films was developed by Thornton in the form of the zone model in figure 3.2.

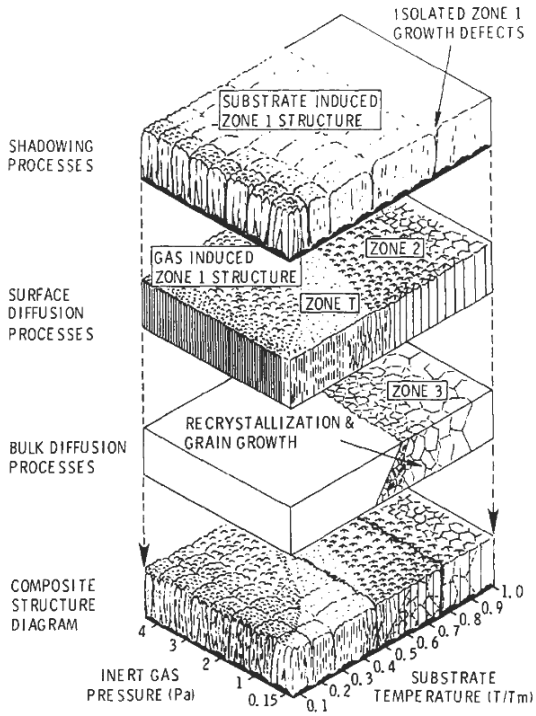

Figure 3.2: General Thornton zone model for sputter deposited metal thin films. The resulting microstructure is dependent on the inert gas pressure, target melting temperature and substrate temperature [15].

Four structural zones are distinguished in figure 3.2: Zone 1, Zone T, Zone 2 and Zone 3. Zone 1 occurs at low T_s/T_m where surface diffusion is negligible and results in voided boundaries and fibrous grains. Amorphous structures may even be observed in this zone. Zone T depicts a dense grain boundary array structure with fibrous grains a hard film with high dislocation density and low ductility. In Zone

2, columnar grains with dense grain boundaries are formed and with a transition to Zone 3, a recrystallised grain structure with low dislocation density manifests [15].

3.3. CHARACTERISATION

3.3.1. SPECTROPHOTOMETRY

The transmittance, reflectance and absorbance of a material as a function of wavelength can be measured using an optical spectrometer. A Perkin Elmer 1050 spectrometer with the ability to determine the total and diffused transmittance and reflectance of a material in the spectral range between 225 nm and 2500 nm was used for analysis in this project. Figure 3.3 illustrates the basic working principle of a spectrometer.

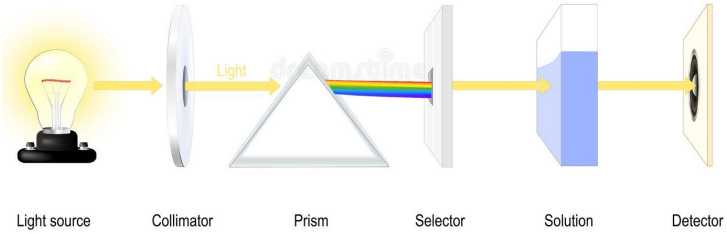

Figure 3.3: Principle of spectrometry [16].

The desired wavelength range of light is produced by a light source. A collimator (lens) transmits a straight beam of light (photons) which then pass through a dispersion device or monochromator (prism) which splits the incidence light into several wavelengths. The wavelength selector transmits only the desired wavelength. After passing through the sample, the absorbed amount of photons is detected. In order to account for light scattering, an integrating sphere as shown in figure 3.4 can be used.

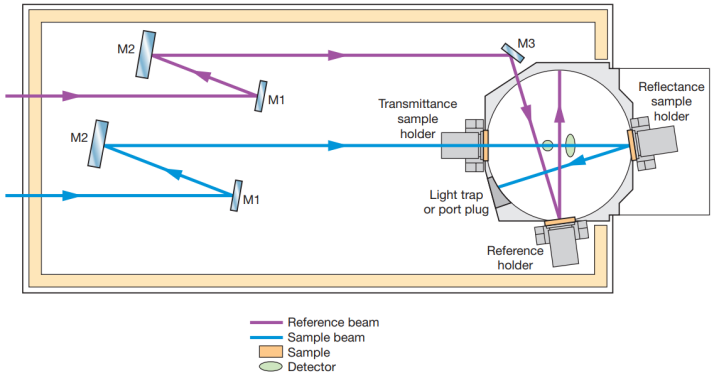

Figure 3.4: Integrating sphere used for spectrophotometry measurements [17].

Due to light scattering taken into consideration, measurements done using integrating spheres are more accurate than standard spectrometers. After obtaining transmittance and reflectance values, the absorbance can be calculated using Kirchhoff's law.

$$Transmittance + Reflectance + Absorbance = 100\% \tag{3.1}$$

Where the values of transmittance, reflectance and absorbance should all be in percentages. According to Beer-Lambert's law, the transmittance and absorbance are related by the ratio of incident and transmitted intensity of light.

$$T = I_t / I_0 = e^{(-\alpha d)} \tag{3.2}$$

Where I_t and I_0 are the respective transmitted and incident light intensity , α is the absorption coefficient and d the sample thickness.

3.3.2. SPECTROSCOPIC ELLIPSOMETRY

Spectroscopic ellipsometry is an optical technique based on the change in the polarization state of light as it is reflected from a sample. Using a modeled approach, this technique can be used to determine the thickness, uniformity, roughness and bandgap among other parameters of a thin films. Figure 3.5 illustrates the working principle of spectroscopic ellipsometry.

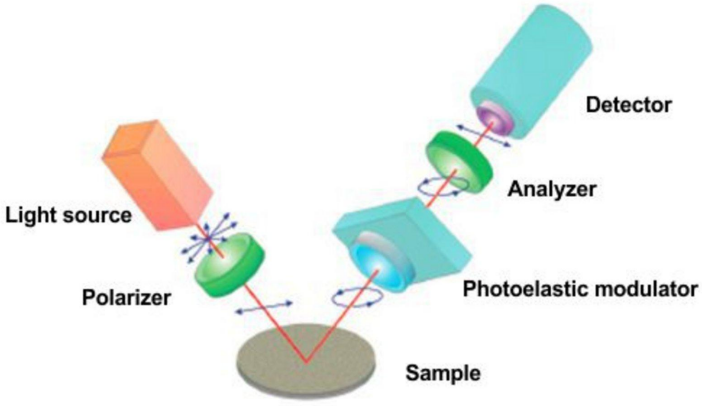

Figure 3.5: Working principle of spectroscopic ellipsometry [18].

Unpolarized light produced from a light source is linearly polarized and reflected off a sample surface. After reflection, the polarization changes to elliptically polarized light. The change in polarization is characterised by parameters Ψ and Δ which are related as follows.

$$\rho = R_p / R_s = tan(\Psi) exp(i\Delta) \tag{3.3}$$

Where R_p is the reflectivity for p-polarized light, R_s the reflectivity for the s-polarized light, Ψ is the magnitude and Δ is the phase difference. An important aspect to keep in mind is that ellipsometry does not measure film thickness and other optical properties directly. An appropriate model must be chosen to fit acquired data in order to obtain the previously mentioned properties. In this work a M-2000DI system (J.A. Woollam Co., Inc.) spectrometer was used for analysis.

3.3.3. MINI RT

Film thickness was also measured by using a Eta-optic mini RT setup, which also requires fitting acquired transmittance and reflectance data using optical modelling. Mini RT measures the wavelength-dependent reflectance and transmittance of a thin film as opposed to spectrophotometry which measures the absolute reflectance and transmittance (spectrophotometry takes scattering into account). Once reflectance and transmittance are measured, the parameters film thickness, plasma frequency and oscillator resonance frequency can be manually adjusted in order to obtain a acceptable fit with low deviation compared to the used model. An automated optimisation procedure varies material properties in the model until measured data and calculated spectra are in agreement.

3.3.4. FOUR-POINT PROBE

Electrical resistivity affects the voltage, capacitance and series resistance of a semiconductor and depends on the doping level and nature of the semiconductor. A four point probe is used to measure sheet resistance which in turn is used to calculate the electrical resistivity of a thin film without any influence of the contact resistance. The working principle of this technique can be seen in the figure 3.6.

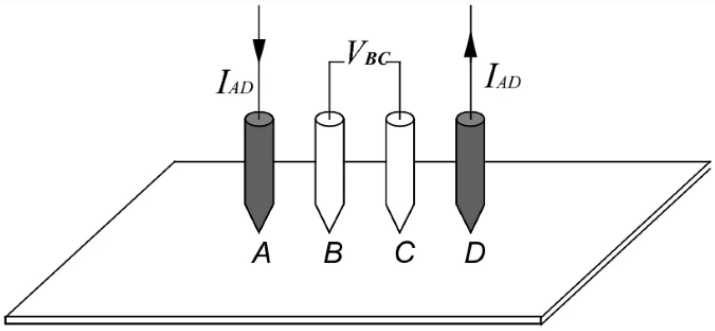

Figure 3.6: Schematic overview of a four point probe [19].

The probe consists of two current carrying probes (A and D) and two voltage measuring probes (B and C). After measuring the current and voltage, the sheet resistance can be calculated as follows.

$$R_{sq} = (U/I) * CF \tag{3.4}$$

Where CF is a correction factor depending on the sample's dimensions. The need for a correction factor is caused by the proximity of a boundary (sample's edges) which limits the current paths in the sample. After obtaining sheet resistance, the thin film electrical resistivity (ρ) can be calculated by multiplying with the sheet thickness.

3.3.5. HALL EFFECT

Carrier density, charge carrier mobility and resistivity are crucial parameters in selecting and processing materials for TCO's and can be quantified using a Hall setup. The working principle of Hall measurements is based on the Lorentz force, the force experienced by an electric charge moving along an electric field in the presence of a magnetic field.

$$\boldsymbol{F} = -q(\boldsymbol{E} + \boldsymbol{v} * \boldsymbol{B}) \tag{3.5}$$

When a magnetic field is applied to a semiconductor, the carriers shift to one side causing a potential drop characterised as the Hall voltage (V_H) which can be positive (p-type semiconductor) or negative (n-type semiconductor). The sheet carrier density can then be calculated using equation 3.6.

$$N_{sheet} = \frac{IB}{e \mid V_H \mid} \tag{3.6}$$

A current is applied (I_{13}) to two opposite corners of the film, while the voltage (V_{24}) is measured across the two remaining corners as seen in figure 3.7.

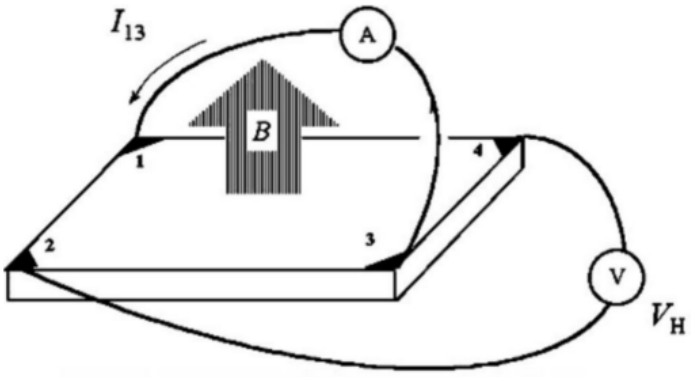

Figure 3.7: Schematic overview Hall measurement [12].

After obtaining the measured voltage, sheet resistance (R_{sh}) can be determined, which is multiplied with the sheet thickness in order to determine sheet resistivity. The sheet resistance and measured Hall voltage can be used in order to determine the mobility as shown in equation 3.7.

$$\mu = \frac{V_H}{R_{sh} IB} \tag{3.7}$$

Where μ is calculated in cm^2/Vs. The resistivity determined from Hall measurements should be consistent with those calculated from four-point probe measurements. In this work negligible discrepancies were found between the measured values. Hall measurements were performed at room temperature with an applied magnetic field of 0,51 T.

3.3.6. X-RAY DIFFRACTION

X-ray diffraction (XRD) analysis is a method of analysing the crystallographic structure of a material by irradiation with incident x-rays followed by measuring

the intensities and scattering angles after interaction with the material. Common applications are the identification of materials based on their diffraction pattern, phase identification and deviation of the actual structure from the ideal one (owing to internal stresses and defects). A regular array of atoms (crystals) scatter incident x-rays primarily through interaction with the atom's electrons, where a regular orientation of atoms produce a regular array of spherical scattered x-rays. The diffraction process is the interference of scattered x-rays either in a constructive or destructive manner, where the former occurs when equation (3.8) known as Bragg's law is satisfied.

$$n\lambda = 2dsin(\theta) \tag{3.8}$$

In equation (3.8), n is an integer, λ is the incident x-ray wavelength, d the spacing between diffraction planes and θ the angle of incident x-rays. In a pollycrystalline material, the possible crystal orientations may be detected by changing θ. Constructive interference results in high intensity's of the reflected x-rays at precise angles. Peak intensity also gives a good indication of the preferred crystal orientation and the degree of crystallinity.

In this work, a Bruker D8 Advance diffractometer with a Co anode and Kα radiation was used for analysis [20].

3.3.7. SCANNING ELECTRON MICROSCOPY

On of the most famous and widely applied thin film characterisation techniques is the scanning electron microscope (SEM). A schematic SEM setup is illustrated in figure 3.8.

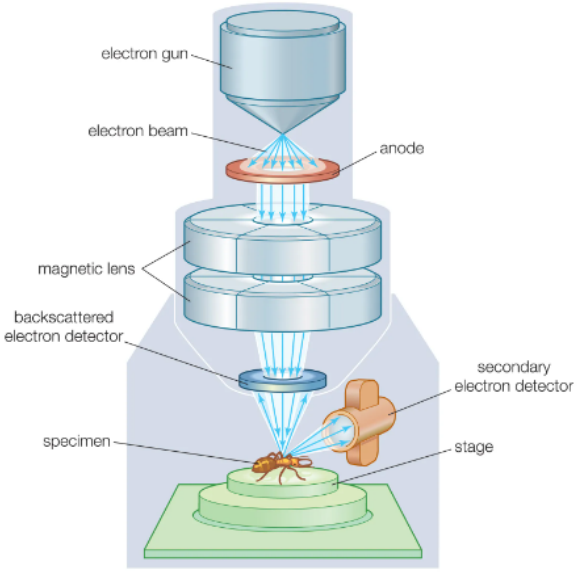

Figure 3.8: Schematic overview of a SEM [21].

Electrons thermoionically generated and emitted from a cathode in the electron gun are drawn to an anode and focused by a series of successive condenser lenses to a very fine spot size (~ 5 nm). The process takes place under vacuum conditions, preventing unwanted, image distorting interference with the electron beam. Pairs of scanning coils located at the final (objective) lens deflect the beam either linearly or in raster fashion over a rectangular area of the specimen surface. Electron beams with energy's from a few thousand up to 50 keV are utilised. Impingement upon the specimen results in deceleration of primary electrons by energy transfer to atomic electrons and the lattice resulting in a multitude of essential electron excitations in the form of secondary electrons (SE) and backscatter electrons (BSE). Additionally, x-rays, photons and heat may also be generated. SE's are low energy electrons, emitted from surface depth sample atoms as a result of inelastic collisions with primary electrons, thus contain more detailed surface information. BSE's are inelastically scattered electrons with essentially the same energy as incident electrons and provide information about the composition in multi-phase samples. The probability backscattering increases with increasing atomic number of the sample [15]. A field-emission scanning electron microscope (FE-SEM) Hitachi Regulus 8230 was used for characterisation of thin films in the research.

3.3.8. THERMAL DESORPTION SPECTROSCOPY

The desorption rate of desorbing gasses from a surface can be measured as a function of temperature using thermal desorption spectroscopy (TDS). The sample is inserted in a vacuum chamber, where it is exposed to a set range temperature or

temperature range. As the temperature increases, the desorption rate of a specific species may increase an be detected. Desorbed gasses are usually detected using a mass spectrometer [22].

In this research a Bruker G8 Galileo setup was used for analysing hydrogen desorption in hydrogen doped indium oxide thin films. The setup is able to detect hydrogen in a measuring range from 0,01-1000 ppm depending on sample weight. In order to detect hydrogen desorption, samples were placed and heated in a quartz tube, where nitrogen carrier gas is used in order to transport desorbed hydrogen to the detector.

4

MAPPING OUT

Thin films with various properties have reportedly been deposited using RF magnetron sputtering still, obtaining the same or even similar properties while applying the reported deposition conditions proved to be challenging. For the purpose of investigating the capability and limitations of the available sputtering equipment, deposition parameters influencing the desired opto-electrical properties were varied in ranges based on previous experiments reporting successful results. The following sections will provide insight into the influence of deposition conditions on the opto-electrical properties of three TCO's: tin doped indium oxide (ITO), hydrogen doped indium oxide (IOH) and intrinsic zinc oxide (i-ZnO). Properties obtained for ITO will be used as reference for comparison to IOH and i-ZnO. The positive and negative properties of these TCO with respect to their deposition conditions will be presented and discussed.

4.1. INDIUM OXIDE

Indium oxide is a wide badgap, n-type semiconductor which can be easily doped. It has a melting temperature of 1910 °C and may be amorphous or crystalline depending on the deposition conditions. In its crystalline form, In_2O_3 may exist either in the metastable rhombohedral -or the stable, more common cubic bixbyite (BCC) structure.

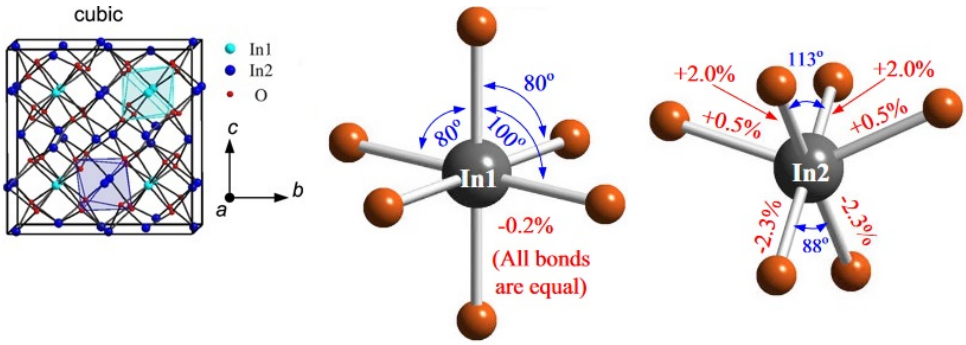

Figure 4.1: Crystal structure of the stable cubic bixbyite structure of In_2O_3 along with possible coordinations In1 and In2. The percentages indicate the difference in bond length compared to the average value of 0,217 nm of all In-O bonds [23] [24].

4

In the cubic bixbyte structure, each unit cell contains 80 atoms, 48 of which are oxygen. Indium atoms have two distinct sites, In1 and In2 as indicated in figure 4.1. Both In1 as well as In2 atoms are bonded to six oxygen atoms however, the In-O bonds for In1 atoms are linear, symmetrical and shorter than the average In-O bond. In_2O_3 in the BCC crystal structure has a lattice parameter of 1,011 nm and a bandgap of ~2,9 eV [12]. Oxygen vacancies have been reported to give rise to the conductivity in undoped In_2O_3 acting as deep donors present in two stable charge states: 2+ and 0. Annealing indium oxide in an oxygen atmosphere results in an increase in electron mobility and a drop in carrier concentration indicating the removal of oxygen vacancies acting as shallow donors. The presence of interstitial oxygen is unlikely as this result in a decreased mobility due to these oxygen atoms behaving as ionized impurities [23].

4.1.1. INDIUM TIN OXIDE (ITO)

Doping indium oxide with tin i.e. replacing some indium atoms with tin atoms, results in the n-type semiconductor indium tin oxide. Currently ITO is one of the most researched and applied TCO's with an estimated global market value of $1,7 billion in 2022. ITO's popularity is attributed to its excellent photoelectric properties such as an average transparency around 89,7% in the visible and near infrared regions, a tunable carrier density up to $10^{21}/cm^3$ and electron mobilities normally in the range of 20-40 cm^2/Vs deposited using methods such as magnetron sputtering, pulsed laser deposition and plasma-enhanced chemical vapour deposition, even reaching up to 62,1 cm^2/Vs using reactive plasma deposition. These relatively high electron mobilities are a result of a highly dispersive and delocalized conduction band minimum, which mainly consists of indium 5s orbitals [25]. The carrier density has its origins to thank to the presence of low formation energy tin-indium antisite and oxygen vacancy defects [26]. Sputtered ITO films can be polycrystalline or

amorphous depending on the deposition conditions. The sputtering process usually takes place at high substrate temperatures (≥200 °C) in order to obtain crystalline films resulting in better transparency and conductivity. ITO deposited at room temperature using RF sputtering has been reported to result in amorphous films with poor electrical and optical properties due to insufficient crystallisation of the film [27]. The following results will discuss the influence of sputtering parameters on the produced ITO films using available RF sputtering equipment. Deposition temperature, time and power were varied in order to illustrate the capabilities and limitations of the equipment.

TEMPERATURE

The influence of substrate temperature on the quality of ITO thin films will be illustrated in this section. Table 4.1 provides an overview of the deposition conditions applied during sputtering. The figures following table 4.1 will be discussed accordingly.

Table 4.1: Substrate temperature varied ITO depositions.

Sample label	T_s(°C)	p (*10^{-2}mbar)	t (s)	P (W)	d (nm)
ITO19	25	1,6	2000	130	110
ITO20	58	1,6	2000	135	110
ITO24	102	1,6	2000	135	113
ITO28	146	1,6	2000	135	110

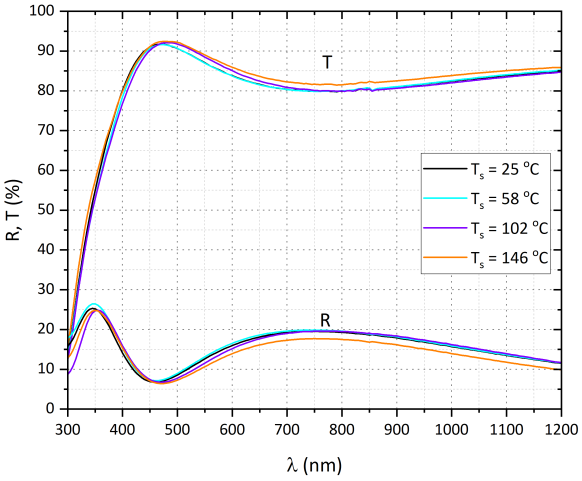

Figure 4.2: Substrate temperature influence on the reflectance and transmittance of resulting ITO thin films. Additional sputtering conditions: p = 1,6*10^{-2} mbar; t = 2000 s; P = 130 W or 135 W.

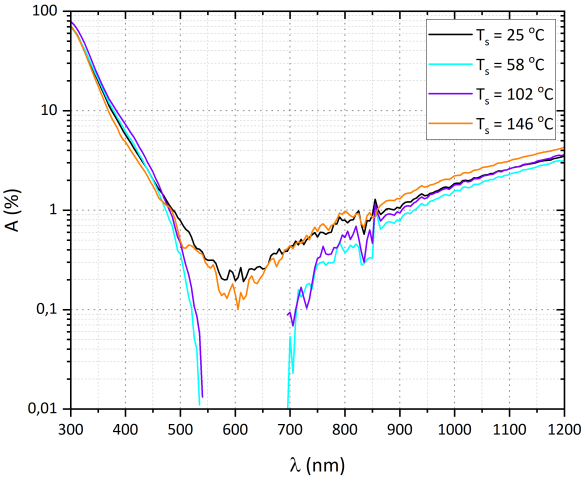

Figure 4.3: Substrate temperature influence on the absorbance of resulting ITO thin films. Additional sputtering conditions: p = 1,6*10^{-2} mbar ; t = 2000 s; P = 130 W or 135 W.

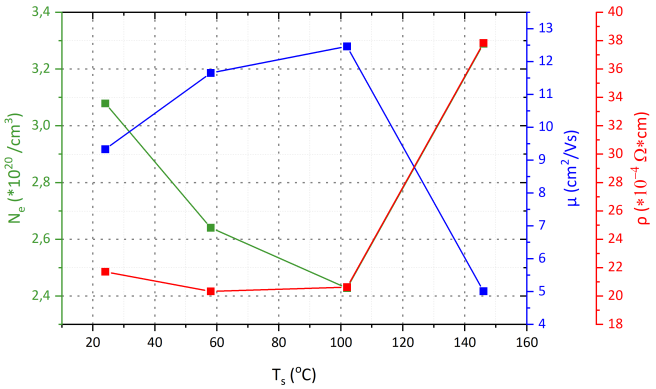

Figure 4.4: Substrate temperature influence on the electrical properties of resulting ITO thin films. Additional sputtering conditions: p = 1,6*10^{-2} mbar ; t = 2000 s; P = 130 W or 135 W.

Figure 4.2 illustrates the influence of deposition temperature on the transmittance and reflectance of ITO films from table 4.1. Overall, the reflectance, transmittance and absorbance are in good agreement between different samples. In the NIR, the film deposited at room temperature is observed to have similar reflectance and transmittance as the films deposited at 58 °C and 102 °C, while the film deposited at 146 °C is observed to have slightly higher transmittance and lower reflectance. At higher deposition temperatures, ITO is suspected to be less amorphous leading to a lower amount of scattering of interacting photons. The sample deposited at the highest temperature of 146 °C is demonstrated to also have the highest NIR absorbance in figure 4.3. The reason for this is the higher amount of charge carriers present in the film deposited at 146 °C. In the visible and UV region, the absorbances for samples deposited at lower temperatures are in agreement with each other.

With increasing temperature, an increase in mobility and decrease in carrier concentration is observed up to 102 °C in figure 4.4, both affecting the resistivity due to its inverse proportional relation to mobility and free carrier concentration. The higher amount of charge carriers at a deposition temperature of 146 °C, leads to the conclusion of a larger amount of defects present in the film most likely due to oxygen vacancies acting as donors, but also as carrier recombination sites. The decrease in mobility is also an indication of a higher amount of defects present in the film structure leading to scattering mechanisms such as grain boundary scattering and ionized impurity scattering. According to figure 3.2, films produced under the deposition conditions in table 4.1 are all highly amorphous, resulting in relatively low mobility and high defect density within the films. In spite of the amorphous, defect filled nature of these films, they have an average transmittance 85-87 % in the visible wavelength region. The films all had similar thicknesses of ~

110 nm, indicating that deposition temperature alone did not have an influence on film thickness.

RF POWER

During depositions, the RF power is a major contributing factor to film quality. This section will demonstrate the influence of deposition power in combination with variable deposition time on the opto-electrical properties of ITO thin films. The applied deposition parameters are displayed in table 4.2.

Table 4.2: RF power and time varied ITO depositions.

Sample label	T_s(°C)	p (*10^{-2}mbar)	t (s)	P (W)	d (nm)
ITO20	58	1,6	2000	135	111
ITO21	58	1,6	1600	190	144
ITO22	58	1,6	1200	245	152
ITO23	58	1,6	800	300	130

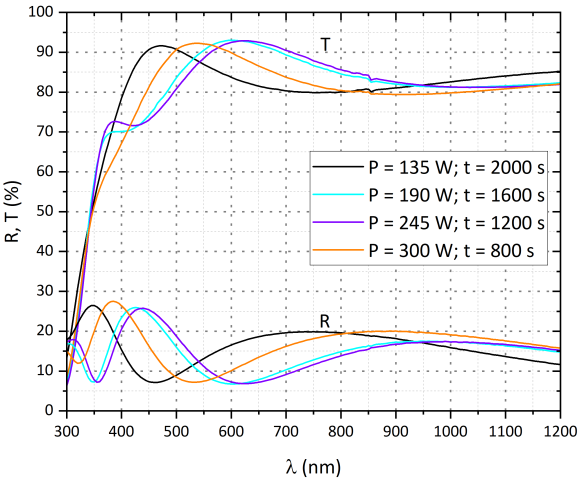

Figure 4.5: Power and time influence on the reflectance and transmittance of resulting ITO thin films. Additional sputtering conditions: T = 58 °C; p = 1,6*10^{-2} mbar.

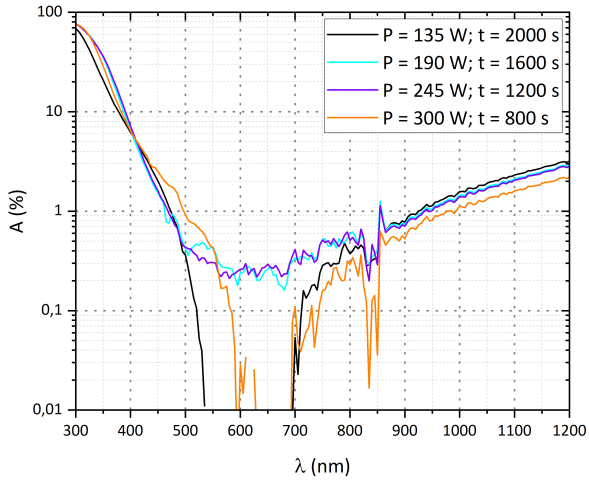

Figure 4.6: Power and time influence on the absorbance of resulting ITO thin films. Additional sputtering conditions: T = 58 °C; p = 1,6*10^{-2} mbar.

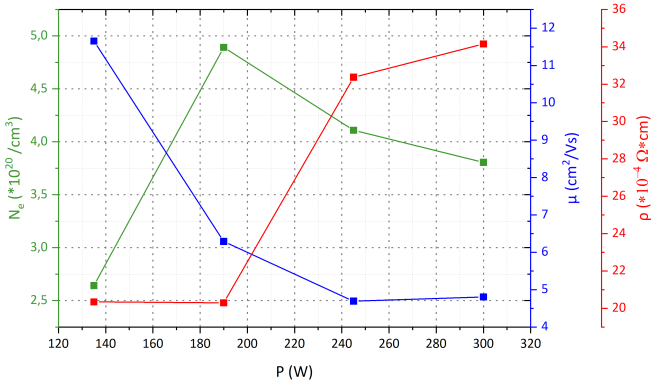

Figure 4.7: Power and time influence on the electrical properties of resulting ITO thin films. Additional sputtering conditions: T = 58 °C; p = 1,6*10^{-2} mbar.

From the properties given in table 4.2, the influence of RF power and deposition time on film thickness is clear. Increased deposition power translates a higher amount of kinetic energy to the sputtered ITO particles leading to a less random orientation and more uniform grain growth resulting in a smoother surface [28]. The increase in kinetic energy leads to a higher amount of atoms being shot loose

from the target and diffusing on to the substrate. Figure 4.5 demonstrates the the transmittance and reflectance performance for the samples in table 4.2. Although there is a 400 second difference in deposition time between ITO21 and ITO22, they have similar reflectance and transmittance across the entire wavelength range with an average transmittance > 80 % in the visible wavelength range. Sample IOT20 which was deposited with the highest deposition time and lowest power stands out compared to the remaining samples with a slightly higher transmittance and lower reflectance in the NIR. The interference fringes in figure 4.5 form as a result of the thickness. Figure 4.6 illustrates the effect of power and deposition time on the absorbance of the films from table 4.2. Absorbance in the NIR appears to decrease slightly with increasing power and decreasing time, while an agreement is reached for the UV region.

Even though a higher deposition power may lead to better quality films, due to a larger amount of collision within the plasma, the amount of collisions with the film surface are increased as well. These collisions may lead to film damage during formation, causing an increase in defect density. Figure 4.7 reflects the effect of increasing power in the electrical properties of the film. Carrier density increases up to a power of 190 W, but decreases with further increase of the power. The decrease in carrier density may be explained by the decrease in oxygen vacancies as donors and the increase in bivalent indium or tin as acceptors. Decreasing deposition time while increasing power may lead to insufficient crystallisation during deposition, resulting in films becoming more amorphous under these conditions. The decreasing mobility with increasing power and decreasing deposition time can be accounted for by negative ion damage of the surface during sputtering [29].

DEPOSITION TIME

The following figures and discussion will give insight on the influence of deposition time on the quality of ITO thin films. Deposition parameters used in order to obtain these films are given in table 4.3.

Table 4.3: Time varied ITO depositions.

Sample label	T_s(°C)	p (*10^{-2}mbar)	t (s)	P (W)	d (nm)
ITO16	25	1,6	800	130	46
ITO17	25	1,6	1200	130	70
ITO18	25	1,6	1600	130	90
ITO19	25	1,6	2000	130	110

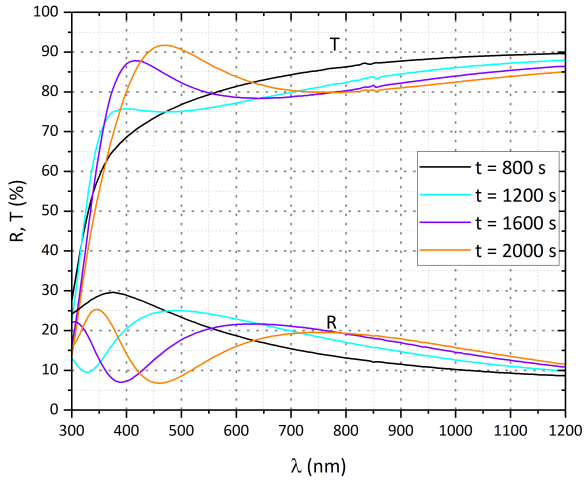

Figure 4.8: Time influence on the reflectance and transmittance of resulting ITO thin films. Additional sputtering conditions: T = 25 °C; p = 1,6*10^{-2} mbar; P = 130 W.

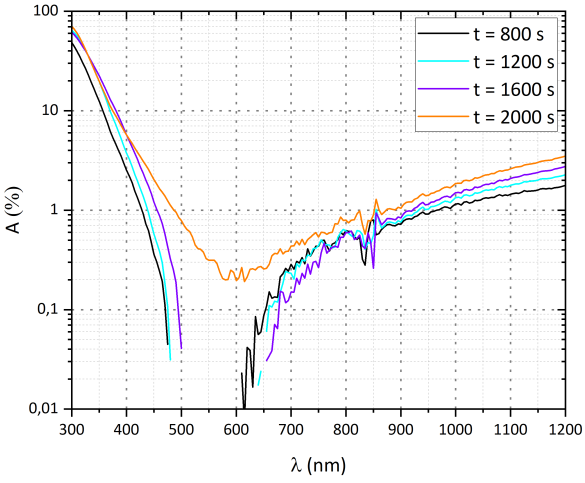

Figure 4.9: Time influence on the absorbance of resulting ITO thin films. Additional sputtering conditions: T = 25 °C; p = 1,6*10^{-2} mbar; P = 130 W.

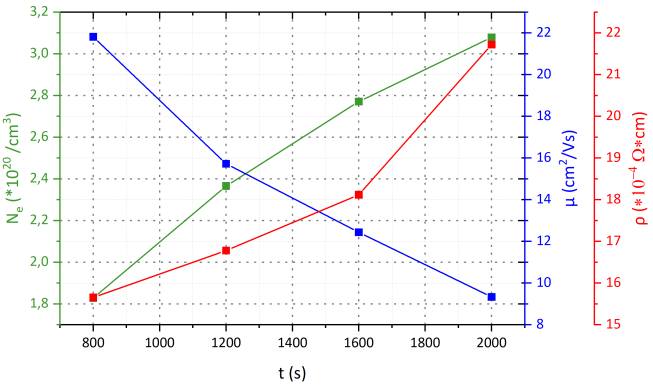

Figure 4.10: Time influence on the electrical properties of resulting ITO thin films. Additional sputtering conditions: T = 25 °C; p = 1,6*10^{-2} mbar; P = 130 W.

From figure 4.8 a clear difference in transmittance and reflectance is observed between the samples with lowest and highest deposition times. These are also the thinnest and thickest samples where the thickest sample of 110 nm is almost 2,5 times as thick as the thinnest sample. Extended deposition times at high temperatures are known to result in thick polycrystalline films with larger grain sizes and higher crystallinity with an increased surface roughness [30] [31]. Although higher deposition times may reduce the amorphous nature of these films, they are still reasoned to be amorphous, because the deposition took place at room temperature. Increasing deposition times result in interference fringes forming (peaks in figure 4.8) in the visible region.

When the UV region is considered, the thicker samples become less transmissive, indicating that the bandgap energy is approached by the energy of incoming light. As the samples get thicker, a slightly lower bandgap is observed as these samples become absorbing at slightly higher wavelengths [30] [32]. Figure 4.9 illustrates the shift in absorbance from thin to thicker samples over the entire wavelength range. In the NIR, parasitic absorption increases with increasing film thickness. This can be explained using figure 4.10, where the carrier density is observed to increase with increasing deposition time. It has been established that samples deposited under exactly the same conditions except for increasing deposition time, tend to become thicker. For thicker samples deposited at room temperature, the defect density increases as a consequence of little to no crystallization leading to larger amount of carrier traps, thus an increasing amount of free carriers is observed. The amorphous nature of the films results in a lower mobility and increased resistivity.

4.1.2. HYDROGEN DOPED INDIUM OXIDE (IOH)

Sputtering In_2O_3 in the presence of water vapour results in a hydrogen doped indium oxide TCO with excellent electrical properties. Films deposited at relatively low deposition temperatures (<200 °C) were reported to posses mobilities >100 cm^2/Vs with carrier concentrations in the range of ~$2*10^{20}/cm^3$ along with optical transparency's of ~ 90% in the visible region. Hydrogen can be present as either interstitial hydrogen (H_i) or substitutional hydrogen (H_O) in the indium oxide crystal lattice. H_i occupies sites in the crystal lattice which are normally unoccupied by the atoms of that structure, while H_O replaces an oxygen atom in the structure. In most cases, H_i is amphoteric, acting as a donor in p-type semiconductors and as an acceptor in n-type semiconductors. The amphoteric nature of H_i means that it cannot be the cause of conductivity, since it self-compensates nonetheless, there are a few exceptional materials where it acts exclusively as a donor such as ZnO and In_2O_3, being the cause for n-type conductivity. Three charge states may be distinguished for interstitial hydrogen: positive, neutral and negative.

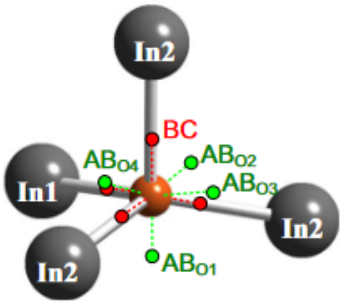

Figure 4.11: Possible occupation sites for H_i^+ in In_2O_3. H_i^+ is not stable at the bond centers (BC), thus the preferred sites are the antibonding sites (AB_O) [24].

H_i^+ prefers sites near the anions and has the lowest formation energy (-2,09 eV) at the antibonding site AB_{O_1} which will be the most likely site of occupation during film growth. Formation energy's at the remaining anitbonding sites are: -1,66 eV at AB_{O_2}; -1,34 eV at AB_{O_3} and -1,35 eV at AB_{O_4}. Neutral and negatively charged H_i have formation energy's > 0 eV, meaning they are far less likely to be present compared to H_i^+. Substitutional hydrogen (H_O) acts exclusively as a donor and always exists in the stable + charge state. H_O^+ has a formation energy of -1,40 eV, which is higher than that of H_i^+, but low enough for a significant incorporation of substitutional hydrogen. Oxygen vacancies act as deep donors in In_2O_3 being present in the 2+ and the neutral charge state with respective formation energy's of -2,68 eV and 0,96 eV. Hydrogen doping eliminates oxygen deficiency's and generates singly charged H^+ donors and reduces carrier scattering leading to an enhancement of carrier mobility [24] [33]. In the following sections, the influence of substrate temperature, RF power, deposition time, water partial vapour pressure and post deposition annealing on the

opto-electrical properties of IOH films will be discussed.

TEMPERATURE

The role of substrate temperature on the quality of IOH films will be analysed using results obtained from the films deposited under conditions supplied in table 4.4.

Table 4.4: Substrate temperature varied IOH depositions.

Sample label	T_s(°C)	p (*10^{-3}mbar)	p_{water}(*10^{-5}mbar)	t (s)	P (W)	d (nm)
IOH44	25	5,7	3	2000	150	176
IOH47	58	5,7	3	2000	150	157
IOH48	124	5,7	3	2000	150	161
IOH50	167	5,7	3	2000	150	173

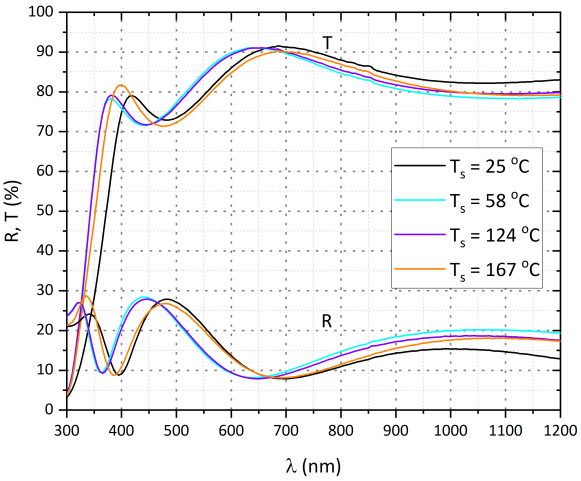

Figure 4.12: Temperature influence on the reflectance and transmittance of resulting IOH thin films. Additional sputtering conditions: p = 5,7*10^{-3} mbar; p_{water} = 3*10^{-5} mbar; t = 2000 s; P = 150 W.

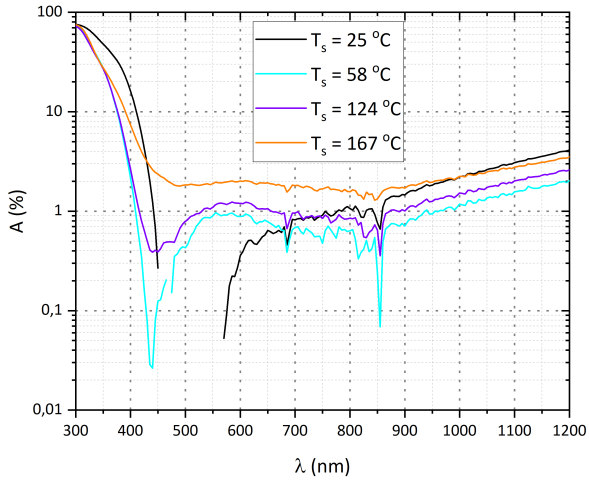

Figure 4.13: Temperature influence on the absorbance of resulting IOH thin films. Additional sputtering conditions: p = 5,7*10^{-3} mbar; p$_{water}$ = 3*10^{-5} mbar; t = 2000 s; P = 150 W.

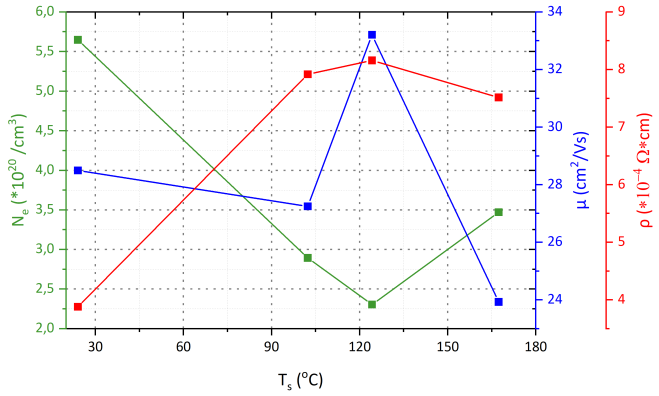

Figure 4.14: Temperature influence on the electrical properties of resulting IOH thin films. Additional sputtering conditions: p = 5,7*10^{-3} mbar; p$_{water}$ = 3*10^{-5} mbar; t = 2000 s; P = 150 W.

In terms of transparency and reflectance in the NIR region, the room temperature deposited film has a slight advantage compared to films deposited at higher temperatures as displayed in figure 4.12. Examining the absorbance in figure 4.13

reveals the room temperature deposited film having the highest absorbance in the NIR, which decreased for the samples deposited at higher temperatures followed by an increase at the highest deposition temperature of 167 °C. The decreasing trend of the carrier density with increasing temperature observed in figure 4.14 supports the decrease in absorbance due to an higher deposition temperature 4.13. The absorbance remains lower than 6% for wavelengths larger than 400 nm. Elevated temperatures are known to produce films with higher crystallinity however, the presence of water vapour during deposition also suppresses lateral grain growth. At higher substrate temperatures during deposition, the amount of defects reduces due to small amounts of crystallisation in the film. The temperature, which hydrogen doped indium oxide was reported to crystallise was around 200 °C for 240 nm thick films. These films are therefore all considered to be amorphous [33] [34][35] [36]. For films deposited at higher temperatures, there appears to be a shift of the bandgap to a higher value. This increase in bandgap value suspected to be caused by the presence of a lower amount of oxygen vacancies and hydrogen interstitials leading to a reversed Moss-Burnstein shift [37]. As explained earlier, a reduction in defects leads to the decrease in carrier concentration. Carrier mobility however, fluctuates due to the amorphous nature of the samples.

RF POWER

The samples which will be discussed in this section have been deposited with increasing power while additional sputtering conditions were kept constant as seen in table 4.5.

Table 4.5: RF power varied IOH depositions.

Sample label	T_s(°C)	p (*10^{-3}mbar)	p_{water}(*10^{-5}mbar)	t (s)	P (W)	d (nm)
IOH1	25	5,7	3	2000	105	118
IOH3	25	5,7	3	2000	130	159
IOH4	25	5,7	3	2000	150	190
IOH6	25	5,7	3	2000	180	237

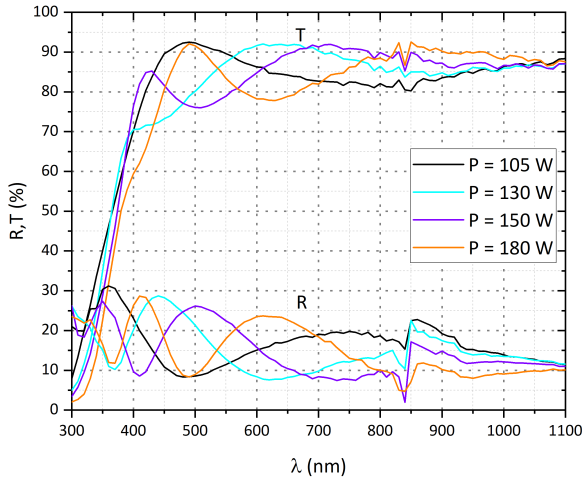

Figure 4.15: RF power influence on the reflectance and transmittance of resulting IOH thin films. Additional sputtering conditions: T_s = 25 °C; p = 5,7*10^{-3} mbar; p_{water} = 3*10^{-5} mbar; t = 2000 s.

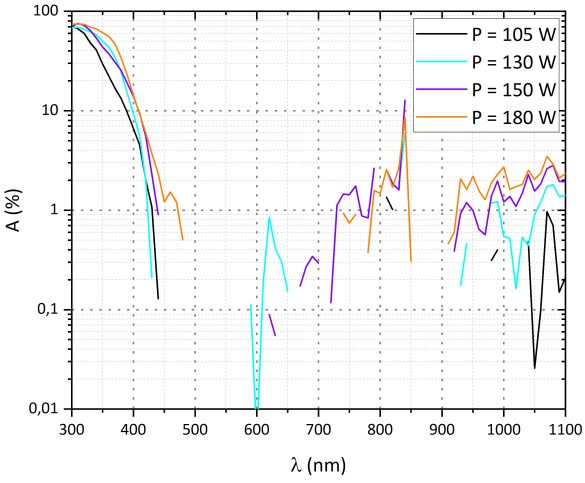

Figure 4.16: RF power influence on the absorbance of resulting IOH thin films. Additional sputtering conditions: T_s = 25 °C; p = 5,7*10^{-3} mbar; p_{water} = 3*10^{-5} mbar; t = 2000 s.

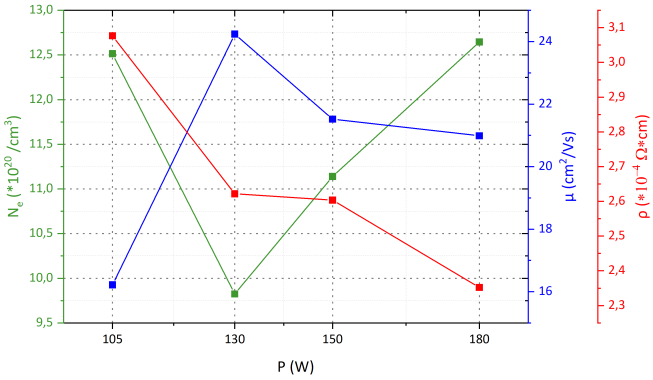

Figure 4.17: RF power influence on the electrical properties of resulting IOH thin films. Additional sputtering conditions: T_s = 25 °C; p = 5,7*10^{-3} mbar; p_{water} = 3*10^{-5} mbar; t = 2000 s.

As mentioned previously, the RF power has significant influence on film thickness observed in table 4.5. The effects of sample thickness are observed from the interference fringes in figure 4.15. In the infrared region, both transmittance and reflectance for all the samples appear to converge, with no agreement between these samples across the remaining wavelength range. From figure 4.16, the NIR absorbance is observed to be the highest for the sample deposited at the highest power leading to the conclusion of a higher carrier density. The kinetic energy translated to the plasma and sputtered In_2O_3 atoms appears to be too small at a RF power of 105 W and too large at 180 W resulting in a higher amount of defects such as vacancies and dangling bonds acting as carrier traps as illustrated by figure 4.17. The carrier density for the sample deposited at the lowest power is almost as high as the carrier density deposited at the highest power, indicating similar doping or similar defect density. Mobility experiences an initial increase when the deposition power is increased from 105 W to 130 W, followed by a slight decrease at higher deposition powers, while the resistivity experiences a decrease. From the discussed figures, it is apparent that a deposition power of 105 W is too low for depositing films possessing the desired opto-electrical qualities.

DEPOSITION TIME

This section will discuss illustrate effect of deposition time on the opto-electrical properties of IOH films, while keeping the all remaining sputtering conditions constant. Samples used for this analysis are displayed in table 4.6.

Table 4.6: Time varied IOH depositions.

Sample label	T_s(°C)	p (*10^{-3}mbar)	p_{water}(*10^{-5}mbar)	t (s)	P (W)	d (nm)
IOH32	25	5,7	3	600	150	42
IOH31	25	5,7	3	800	150	64
IOH30	25	5,7	3	1000	150	85
IOH29	25	5,7	3	1400	150	127

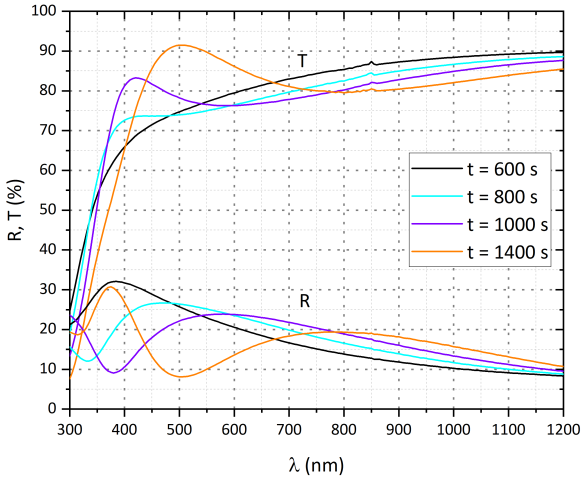

Figure 4.18: Deposition time influence on the reflectance and transmittance of resulting IOH thin films. Additional sputtering conditions: T_s = 25 °C; p = 5,7*10^{-3} mbar; p_{water} = 3*10^{-5} mbar; P = 150 W.

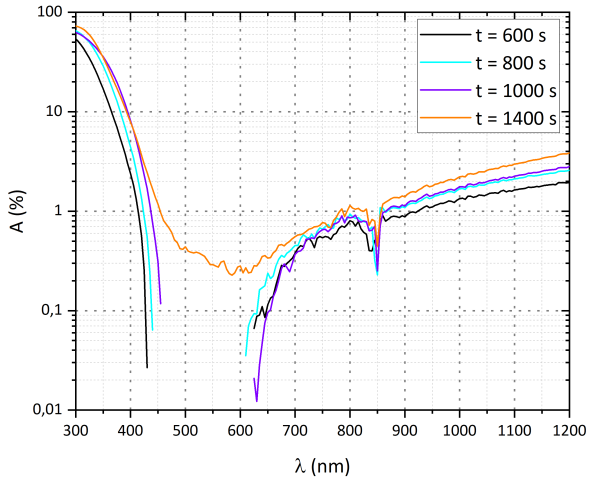

Figure 4.19: Deposition time influence on the absorbance of resulting IOH thin films. Additional sputtering conditions: T_s = 25 °C; p = 5,7*10^{-3} mbar; p_{water} = 3*10^{-5} mbar; P = 150 W.

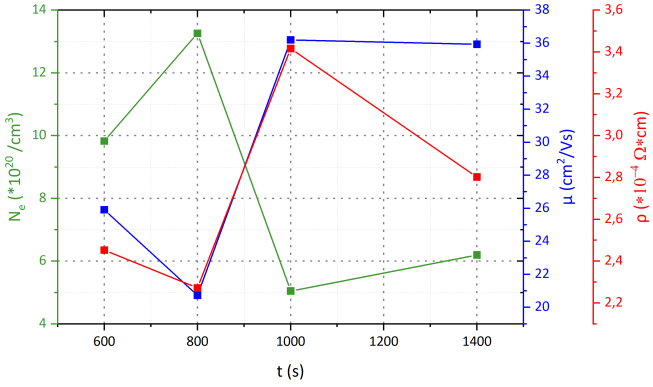

Figure 4.20: Deposition time influence on the electrical properties of resulting IOH thin films. Additional sputtering conditions: T_s = 25 °C; p = 5,7*10^{-3} mbar; p_{water} = 3*10^{-5} mbar; P = 150 W.

Figure 4.18 displays the effect of deposition time on reflectance and transmittance. As the deposition time increases, the sample thickness increases as well resulting in the formation of interference fringes. A shift in bandgap is observed due

to the Moss-Burnstein effect, where the lowest deposition time resulted in the sample with the highest bandgap, while the highest deposition time resulted in the lowest bandgap sample. The thinnest sample also experiences the highest NIR transmittance, lowest NIR reflectance and lowest NIR absorbance. An increase in deposition time i.e. an increase in sample thickness effects all these properties accordingly. The absorption in the NIR increases with sample thickness leading to the conclusion that the carrier density should also increase accordingly. The measured carrier density's for these films however, contradict this statement as can be seen in figure 4.20. Longer deposition times are known to result in higher crystallinity, thus decreasing the amount of defects present in the structure. Carrier mobility increases with increasing deposition time, indicating a lower amount of carrier scattering. These depositions took place at room temperature and are therefore all considered to be amorphous with a high defect density, which explains the irregularity in the measured electrical properties.

H_2O PARTIAL PRESSURE

The samples to be discussed in this section were deposited at a constant deposition temperature, power and deposition time, while the partial water vapour pressure was increased. Deposition conditions for these films can be found in table 4.7.

Table 4.7: H_2O partial pressure varied IOH depositions.

Sample label	T_s(°C)	p (*10^{-3}mbar)	p_{water}(*10^{-5}mbar)	t (s)	P (W)	d (nm)
IOH24	25	5,7	1	1200	150	110
IOH25	25	5,7	2	1200	150	114
IOH26	25	5,7	3	1200	150	109
IOH27	25	5,7	4	1200	150	115
IOH28	25	5,7	5	1200	150	109

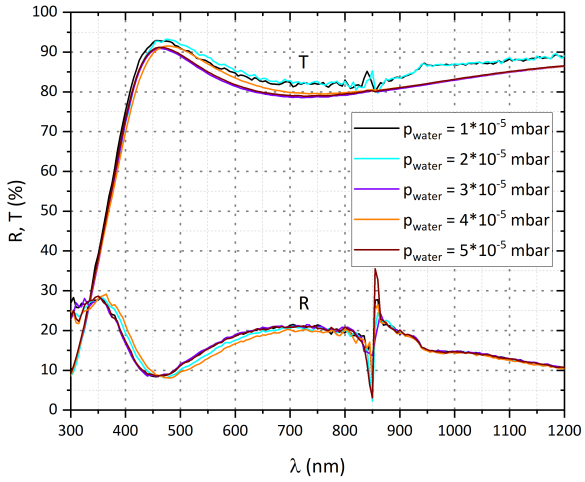

Figure 4.21: Partial water vapour pressure influence on the reflectance and transmittance of resulting IOH thin films. Additional sputtering conditions: T_s = 25 °C; p = 5,7*10^{-3} mbar; t = 1200 s; P = 150 W.

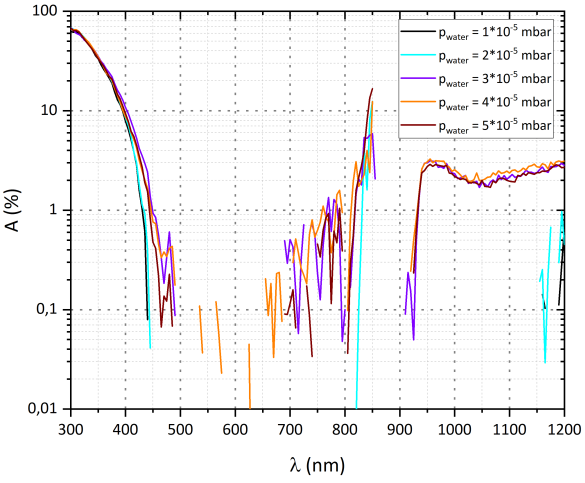

Figure 4.22: Partial water vapour pressure influence on the absorbance of resulting IOH thin films. Additional sputtering conditions: T_s = 25 °C; p = 5,7 *10^{-3} mbar; t = 1200 s; P = 150 W.

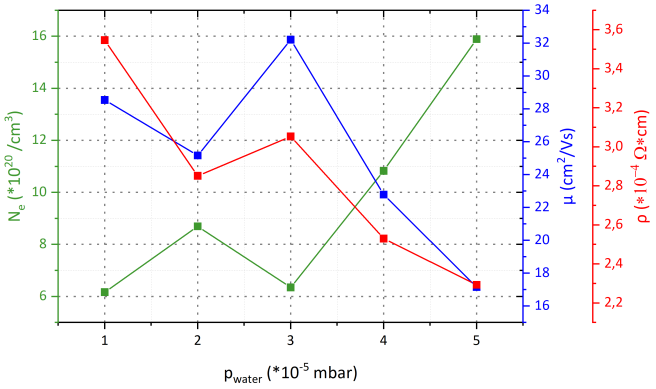

Figure 4.23: Partial water vapour pressure influence on the electrical properties of resulting IOH thin films. Additional sputtering conditions: T_s = 25 °C; p = 5,7*10^{-3} mbar; t = 1200 s; P = 150 W.

The effect of partial water vapour pressure increase on the transmittance and reflectance of the films is illustrated in figure 4.21. The films deposited using the two lowest water vapour pressures have higher overall transmittance especially in the NIR pointing to lower amounts of doping. Increasing the partial water vapour pressure results in a solid agreement between films in terms of transparency. When the absorbance is considered in figure 4.22, a similar effect of low doping is clearly visible in the NIR as well. Structural properties as a result of partial water vapour pressure can be categorised in three groups:

- Group I: $p_{water} \leq 1*10^{-7}$ mbar
- Group II: $5*10^{-7}$ mbar $\leq p_{water} \geq 5*10^{-5}$ mbar
- Group III: $p_{water} \geq 10*10^{-5}$ mbar

Group II was found to produce amorphous films, while group I and III were found to produce polycrystalline films [34] [35]. The higher mobility observed at a partial water vapour pressure of $3*10^{-5}$ mbar combined with the increase in carrier density in figure 4.23 illustrates the doping effect of water vapour during deposition. At higher vapour pressures, carrier mobility starts to decrease, while carrier density experiences a stronger increase pointing out the detrimental effects of too high of a vapour pressure. This effect is most likely attributed to an increased amount of hydrogen in the crystal structure leading to a reduction of indium and oxygen, suppressing grain growth [34] [38]. In the presence of water, the growing In_2O_3 film contains hydroxyl groups known to stipulate the amorphous state [36].

The highest mobility and lowest carrier density are observed at a water vapour pressure of $3*10^{-5}$ mbar in figure 4.23. At water vapour pressures higher than $3*10^{-5}$ mbar, there is a decrease in mobility due to the increased doping leading to a higher

carrier concentration. The increased vapour pressure along with room temperature deposition leads to highly amorphous, defect filled films.

POST DEPOSITION ANNEALING

Solid phase crystallisation by post deposition annealing (PDA) has been known to enhance electrical properties for TCO's i.e. decreased carrier concentration therefore decreasing absorption in the NIR and increased carrier mobility. The reasoning behind the enhancement is the facilitation of grain growth resulting in a reduction of grain boundaries. During annealing, oxygen vacancies are accommodated due to oxygen diffusion and dangling bonds acting as trap states within the bandgap are passivated. This section will demonstrate the effect of PDA on the electrical properties and the NIR absorbance as well as provide a suitable annealing time and temperature.

In order to find the appropriate annealing conditions, samples deposited under the conditions illustrated in table 4.8 were exposed to annealing temperatures from 100 °C to 300 °C with 50 °C increments and held at each temperature for 20 minutes respectively in an ambient atmosphere.

Table 4.8: Post deposition annealed IOH samples.

Sample label	T_s(°C)	p (*10^{-3}mbar)	p_{water}(*10^{-5}mbar)	t (s)	P (W)	d (nm)
IOH44	25	5,7	3	2000	150	160
IOH46	80	5,7	3	2000	150	160
IOH48	124	5,7	3	2000	150	160
IOH49	146	5,7	3	2000	150	160

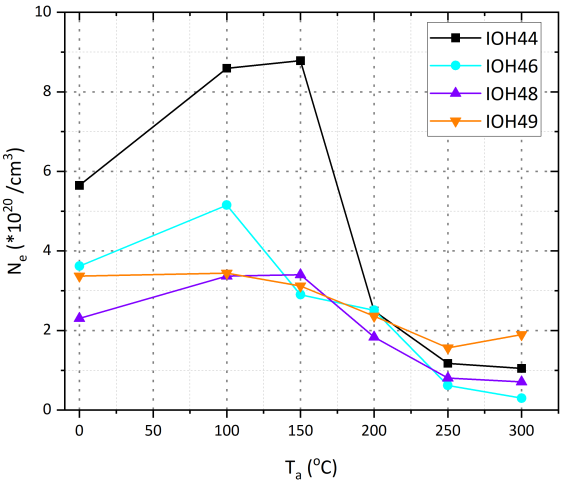

Figure 4.24: Effect of annealing temperature on the carrier density of IOH, annealed for 20 minutes at each temperature respectively.

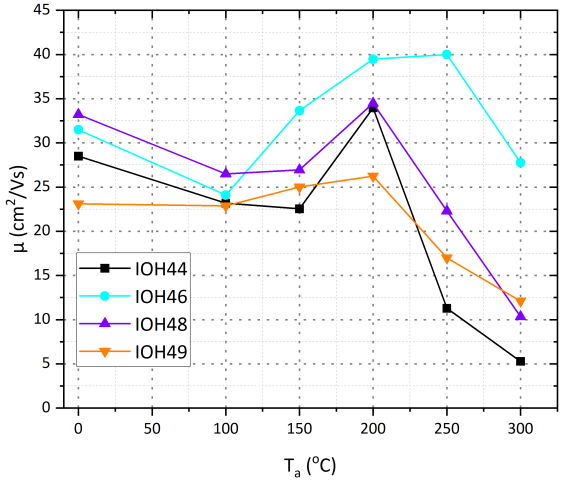

Figure 4.25: Effect of annealing temperature on the carrier mobility of IOH, annealed for 20 minutes at each temperature respectively.

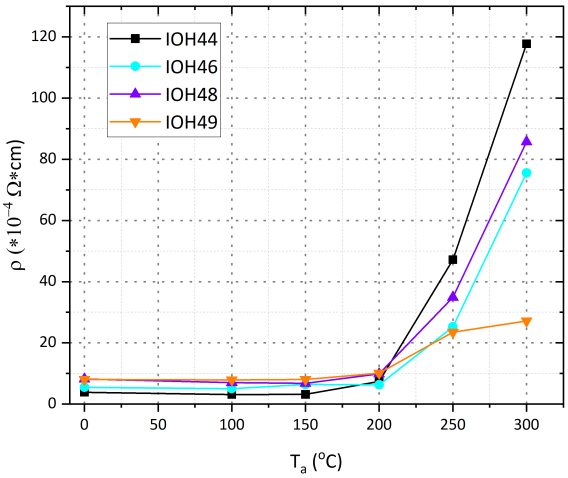

Figure 4.26: Effect of annealing temperature on the resistivity of IOH, annealed for 20 minutes at each temperature respectively.

A clear observation from the figures are the peak carrier mobilities at an annealing temperature of 200 °C. As the annealing temperature is increased to 250 °C and higher, carrier mobilities (figure 4.25) are demonstrated to decrease. A possibility of the decrease in mobility is the introduction of structural defects by keeping the IOH films at these temperatures for 20 minutes. Carrier density (figure 4.24) initially experiences an increase up to annealing temperatures of 150 °C followed by a decrease at annealing temperatures >150 °C nearing a plateau between 250 °C and 300 °C. Up to 200°C, the resistivity (figure 4.26) experiences minimal change, however the decrease in mobility and free carrier concentration at annealing temperatures of 250 °C and 300 °C result in a massive increase in resistivity compared to the initial one.

Small increases were made to find an optimum annealing temperature of 215 °C. Samples were kept at an annealing temperature of 215 °C with intervals of 20 minutes up to 80 minutes in order to find an optimum annealing time, however no notable improvements were observed for annealing times longer than 20 minutes. PDA proved to have significant impact on the opto-electrical properties of IOH thin films when annealed at 215 °C for 20 minutes.

Further annealing experiments at 215 °C with an annealing time of 20 minutes were performed on samples deposited under various conditions in order to observe the annealing effect. The highest mobility of 71,60 cm^2/Vs with a carrier density of $3*10^{20}/cm^3$ and resistivity of $2{,}90*10^{-4}$ Ω*cm were found for samples deposited under the conditions mentioned in table 4.9.

Table 4.9: Highest mobility sample

Sample label	T_s(°C)	p (*10^{-3}mbar)	p_{water}(*10^{-5}mbar)	t (s)	P (W)	d (nm)
IOH4	25	5,7	3	2000	150	160

Room temperature depositions were found to have a better response to PDA treatments compared to samples deposited on heated substrates. The amorphous state upon deposition may be the cause, resulting in better total crystallisation when annealed post deposition. Samples deposited on to heated substrates may experience some crystallisation on parts of the film upon deposition; nonetheless, they retain an amorphous nature overall. PDA for these samples do not result in mobilities higher than 50 cm^2/Vs with carrier density of 1,5*10^{20}/cm^3 and resistivities of 9,60*10^{-4} Ω*cm).

4.2. INTRINSIC ZINC OXIDE (I-ZNO)

Zinc oxide is a semiconductor with a direct bandgap ranging from 3,2 eV at room temperature to 3,44 eV at 4 K and a large excitation binding energy of 60 meV. It is the hardest of the II-VI semiconductors due to its high melting point of 1975 °C and large cohesive energy of 1,89 eV, increasing its resistant to wear. ZnO may crystallize in two different forms: the hexagonal wurtzite structure and the rocksalt structure. The wurtzite structure is thermodynamically stable and widely applied in the thin film industry [39] [40].

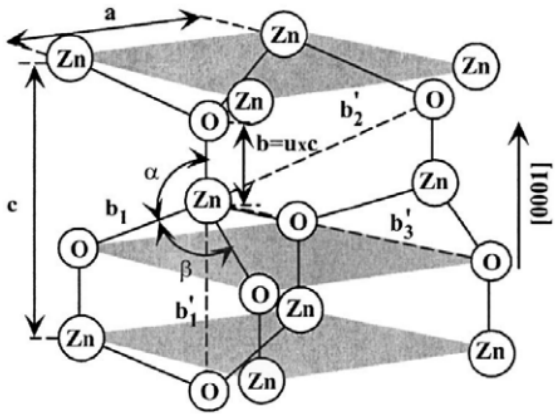

Figure 4.27: Schematic representation of ZnO in a hexagonal wurtzite structure with lattice constants a and c. The parameter u is the bond length or nearest-neighbour distance. α and β (109,47 °in ideal crystal) are the bond angles [39].

Figure 4.27 represents the wurtzite structure of ZnO with lattice constants a = 0,325 nm and c = 0,521 nm. i-ZnO thin films are reported to have an optical transparency of around 90%. As for the electrical properties, sputtered i-ZnO has a relatively low mobility ~10 cm^2/Vs however, since it is undoped, the charge carrier concentration is in the order of ~10^{18} $/cm^3$ [41]. Pollycrystalline i-ZnO has been reported to have a preferential growth along the (002) or c-axis, which has the lowest surface free energy and is perpendicular to the surface. Growth of ZnO along the (100) plane, which has a higher surface free energy has also been established. An intrinsic n-type conductivity of ZnO is attributed to donors from native defects such as oxygen vacancies and zinc interstitials as well as foreign defects in the form of hydrogen interstitials in the crystal structure. Native defects do not provide a sufficiently high concentration of shallow donors, leading to a low conductivity of ZnO thin films [42]. Mobilities >100 cm^2/Vs have been achieved for ZnO films deposited using methods such as pulsed laser deposition and molecular beam epitaxy [43]. Due to its high abundance, low cost, non-toxicity, easy production and high chemical and thermal stability along with relatively good optical properties, i-ZnO proves to be a promising TCO candidate. The following sections will provide some insight into the influence of sputtering properties on the opto-electrical properties of i-ZnO with respect to deposition temperature, RF deposition power and deposition time.

TEMPERATURE

The effect of substrate temperature on the opto-electrical properties of i-ZnO will be discussed in this section. Samples were deposited under the conditions mentioned in table 4.10.

Table 4.10: Substrate temperature varied i-ZnO depositions.

Sample label	T_s(°C)	p (*10^{-3}mbar)	t (s)	P (W)	d (nm)
ZnO23	95	2,6	3600	200	425
ZnO3	126	2,6	3600	200	414
ZnO7	157	2,6	3600	200	374
ZnO19	218	2,6	3600	200	341

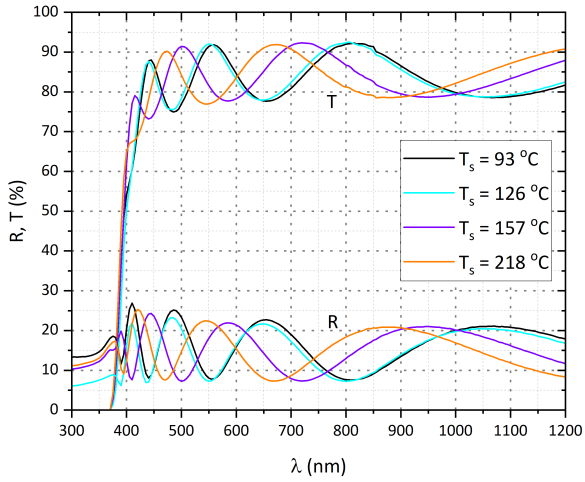

Figure 4.28: Temperature influence on the reflectance and transmittance of i-ZnO thin films. Additional sputtering conditions: p = 2,6*10^{-3} mbar; t = 3600 s; P = 200 W.

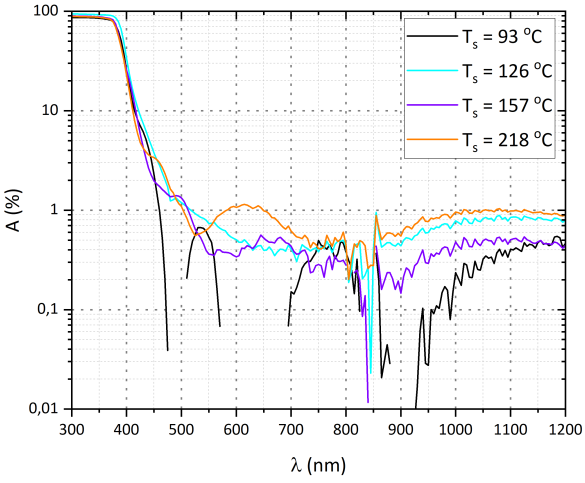

Figure 4.29: Temperature influence on the absorbance i-ZnO thin films. Additional sputtering conditions: p = 2,6*10^{-3} mbar; t = 3600 s; P = 200 W.

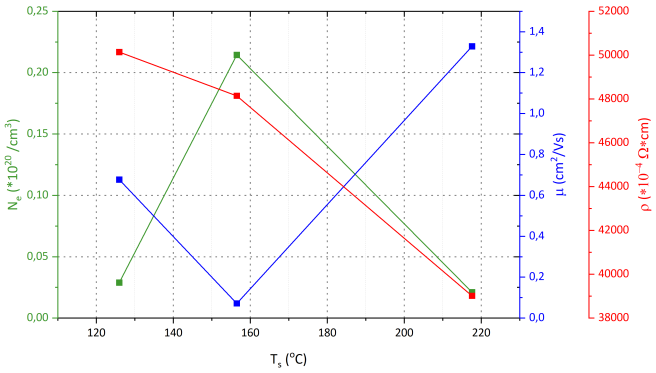

Figure 4.30: Temperature influence on the electrical properties i-ZnO thin films. Additional sputtering conditions: p = 2,6*10^{-3} mbar; t = 3600 s; P = 200 W.

Figure 4.28 illustrates the transmittance and reflectance of i-ZnO films deposited at different substrate temperatures. Many interference fringes are present as a result of the layer thickness are observed in both the reflectance and transmittance. As the temperature increases, a Moss-Burnstein shift is observed. i-ZnO is crystalline as deposited, so an increased substrate temperature during deposition should enhance grain growth. Increasing substrate temperature is observed to have a decreasing effect on substrate thickness.

An interesting observation from the absorbance of these films as displayed in figure 4.29, is the absorbance <1% over a large part of the measured wavelength. For wavelengths smaller than λ = 500 nm, the photon energy nears the bandgap energy for all the films and they become almost completely absorbing. As the substrate temperature increases, there is an increase in absorbance in the NIR, still remaining ~1%. As the substrate temperature increases from 93 °C to 126 °C, an increase in carrier density is observed in figure 4.30, leading to increased NIR absorption. As the temperature is increased further, the carrier density decreases again. Due to the columnar microstructure of i-ZnO deposited on glass, measuring electrical properties proved challenging if not immeasurable. Figure 4.31 illustrates a cross sectional SEM for sample ZnO23 in order to provide support in explaining the electrical properties measured and presented in figure 4.30. Due to its intrinsic nature, carrier density's no higher than 0,21*10^{20}/cm^3 are observed for i-ZnO.

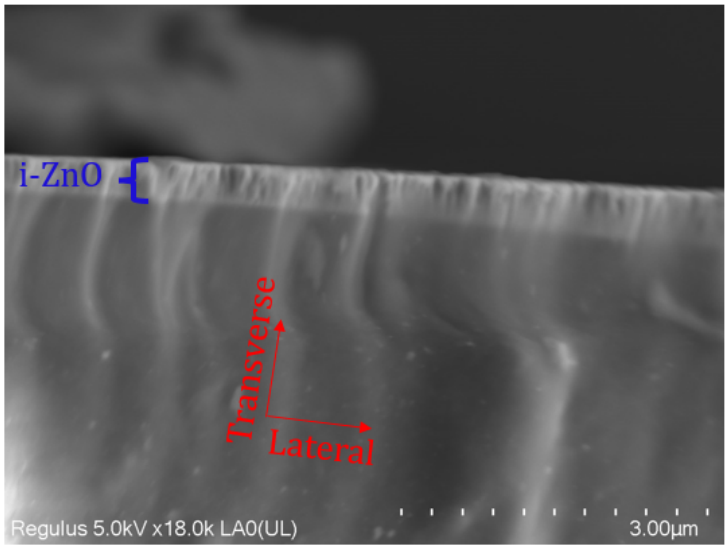

Figure 4.31: SEM cross section of ZnO23. Columnar grains result in high lateral resistance along current path.

The microstructure of i-ZnO films as displayed in figure 4.31 leads to high resistivity in the lateral direction, resulting in low carrier mobilities as confirmed by observing these properties in figure 4.30. As the substrate temperature during deposition increases, some decrease is observed in lateral resistivity. The mobility experiences a slight decrease followed by an increase, while the opposite happens for carrier density. Increased temperature amplifies grain growth, resulting in a lower amount of grain boundaries resulting in less lateral resistance for carriers to encounter. Even so, electrical properties of i-ZnO have been inconsistent with repeated depositions and are unfavourable in comparison to those of ITO and IOH.

RF POWER

The influence of RF deposition power on the opto-electrical properties of i-ZnO will be discussed in this section. An overview of the deposited and analysed samples is presented in table 4.11.

Table 4.11: RF power varied i-ZnO depositions.

Sample label	T_s(°C)	p (*10^{-3}mbar)	t (s)	P (W)	d (nm)
ZnO4	126	2,6	3600	100	133
ZnO3	126	2,6	3600	200	414
ZnO2	126	2,6	3600	300	735
ZnO1	126	2,6	3600	400	910

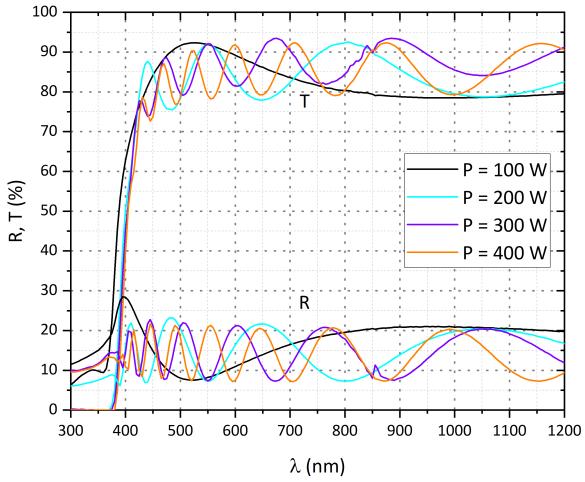

Figure 4.32: RF power influence on the reflectance and transmittance of i-ZnO thin films. Additional sputtering conditions: T_s = 126 °C; p = 2,6*10^{-3} mbar; t = 3600 s.

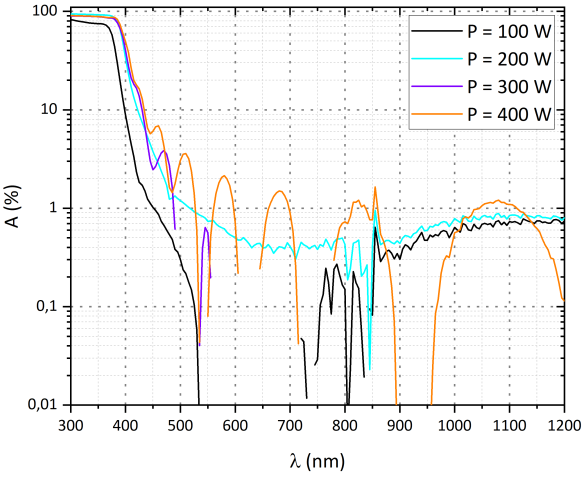

Figure 4.33: RF power influence on the absorbance of i-ZnO thin films. Additional sputtering conditions: T_s = 126 °C; p = 2,6*10^{-3} mbar; t = 3600 s.

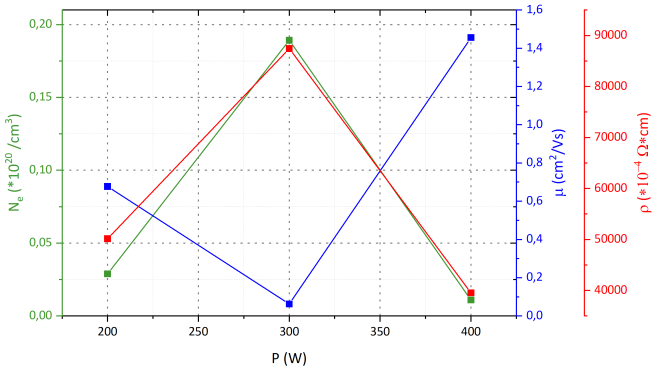

Figure 4.34: RF power influence on the electrical properties of i-ZnO thin films. Additional sputtering conditions: T_s = 126 °C; p = 2,6*10^{-3} mbar; t = 3600 s.

As demonstrated in previous sections, the RF power has an influence on the thickness of the forming film. The transmittance reaches 90% for a large part of the measured wavelength range, while the resistance remains close to or <20%. i-ZnO films however experience a stronger increase in thickness due to an increase in power compared to previously mentioned TCO's. Increasing RF power results in a higher energy transfer to argon ions resulting in an increased amount of bombardment on to the target. The effect of increasing power and thus thickness can be seen in the increased amount of interference fringes present in figure 4.32. In spite of the thickness, these samples have a transmittance close to 90% over a large part of the measured wavelength range.

The absorbances for the samples from table 4.11 are displayed in figure 4.33. It is worth mentioning that the absorbance remains <1% for samples deposited using a RF power up to 300 W and is only slightly higher than 1% for some wavelength ranges for the 400 W sample. Even though these sample thicknesses are in the order of microns, the absorbance remains close to 1%.

With increased power, grain size is known to decrease due to the higher amount of atoms diffusing on to the substrate increasing the probability of forming nuclei. Increased amounts of nuclei allows more grain growth sites resulting in smaller grains, thus more grain boundary's forming [44]. The electrical properties for i-ZnO deposited on a glass substrate fluctuate due to an increase in RF power, not being representative to support the previously made statement.

DEPOSITION TIME

Increasing deposition time has been demonstrated to produce thicker films with high crystallinity and containing less defects compared to amorphous films. In order

to demonstrate the effect of deposition time on crystalline i-ZnO films, the samples as presented in table 4.12 were deposited and analysed.

Table 4.12: Time varied i-ZnO depositions.

Sample label	T_s(°C)	p (*10^{-3}mbar)	t (s)	P (W)	d (nm)
ZnO12	157	2,6	400	300	56
ZnO11	157	2,6	1200	300	219
ZnO10	157	2,6	2000	300	370
ZnO9	157	2,6	2800	300	512

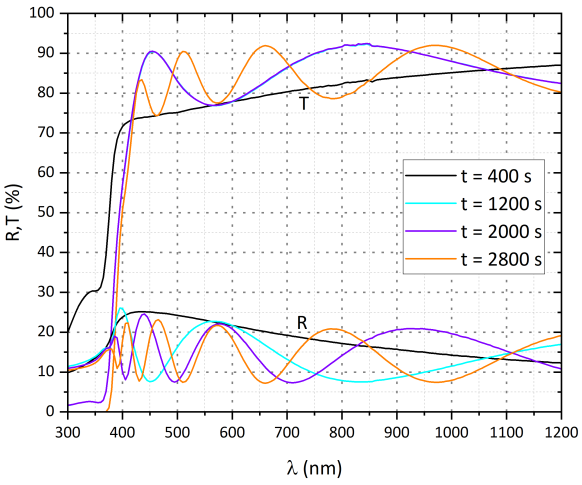

Figure 4.35: Deposition time influence on the reflectance and transmittance of i-ZnO thin films. Additional sputtering conditions: T_s = 157 °C; p = 2,6*10^{-3} mbar; P = 300 W.

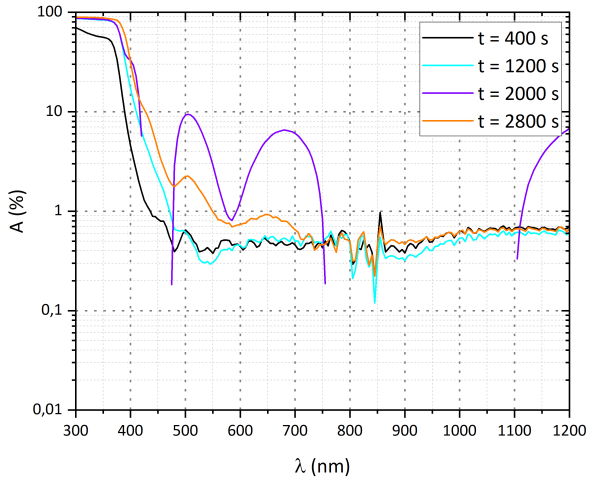

Figure 4.36: Deposition time influence on the absorbance of i-ZnO thin films. Additional sputtering conditions: T_s = 157 °C; p = 2,6*10^{-3} mbar; P = 300 W.

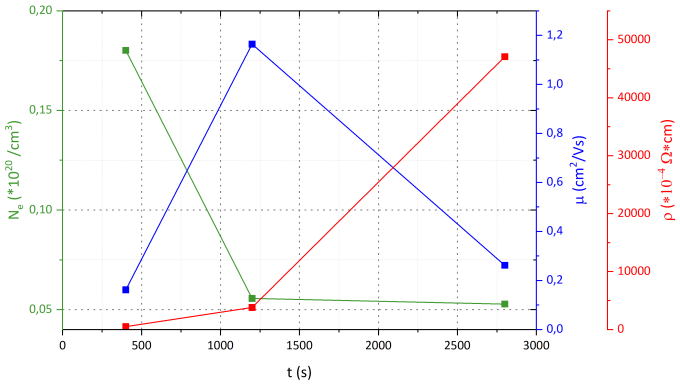

Figure 4.37: Deposition time influence on the electrical properties of i-ZnO thin films. Additional sputtering conditions: T_s = 157 °C; p = 2,6*10^{-3} mbar; P = 300 W.

An increase of deposition time has similar effect on i-ZnO as presented for previous TCO's i.e. an increase in thickness (and decrease in defects at higher temperatures). Transmittance is observed to increase with increasing thickness, while reflectance

decreases. The absorbance again remains below 1% in a large wavelength range for all samples with an exception for the sample deposited for 2000 s. This sample experiences an increase in absorption which is likely caused by defects in the crystal structure. Electrical properties of this sample were not properly measurable and are therefore excluded in figure 4.37. A decrease in carrier density observed from the electrical properties due to increasing deposition time, while mobility experiences a small increase before decreasing. The resistivity keeps increasing, pointing out an increasing lateral resistance indicating structural defects present in the film at a substrate temperature of 157 °C.

5

BI-LAYER

The trade-off between high conductivity and low absorption in the NIR has been emphasised in section 2 of this paper. A well functioning TCO for pv application is one where there is a substantial amount of free carriers available with high lateral electron mobility in such a way that the conductivity given in equation (2.8) is maximised, while the free carrier absorption given in equation (2.12) is kept as low as possible. From previous sections, IOH has been demonstrated to surpass the traditional ITO substantially in terms of free carrier concentration as well as carrier mobility, however parasitic absorption in the NIR was still comparable. i-ZnO has been demonstrated to posses substantially low NIR absorption compared to both ITO and IOH, although retained poor to almost no lateral conducting properties due to the microstructure formed resistance. In pursuance of a TCO surpassing both the electrical as well as optical properties of ITO, the creation of a combined so called bi-layer TCO has been attempted consisting of IOH and i-ZnO. The following section will provide guidance through the selection and optimisation processes in order to obtain functional bi-layers.

5.1. SELECTION

Sample selection for the bi-layer will be discussed in this section. A demonstration of the NIR superiority in terms of absorbance for i-ZnO is provided in figure 5.1.

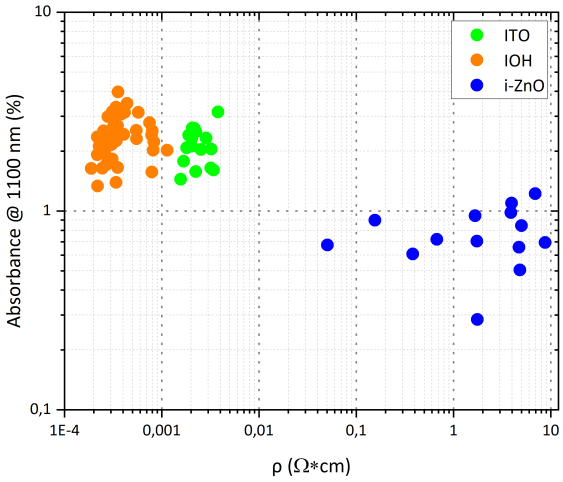

Figure 5.1: Absorbance at 1100 nm vs. resistivity comparison for ITO, IOH and i-ZnO.

The absorbance in the NIR at 1100 nm is close to or even lower than 1% for i-ZnO, while IOH and ITO have absorbances >1%. Even though the lateral resistivity for i-ZnO is much higher, in terms of low parasitic absorption in the NIR, it is clearly the superior TCO. The bottom left corner of figure 5.1 is the desirable area for a well working TCO. The lowest NIR absorption for i-ZnO and the highest mobility for IOH were obtained from the samples deposited under conditions given in table 5.1.

Table 5.1: Sample selection for bi-layer.

Sample label	T_s(°C)	p (*10^{-3}mbar)	p_{water}(*10^{-5}mbar)	t (s)	P (W)	d (nm)
IOH4	25	5,7	3	2000	150	190
ZnO23	95	2,6	-	3600	200	425

According to the findings presented and discussed in the previous chapter, deposition time has a strong influence on film thickness for the samples mentioned in table 5.1. For the purpose of competing with the commercial TCO layer developed and processed at Hyet Solar, the overall thickness should not exceed 700 nm. Deposition rates were calculated and deposition time was altered for depositing individual layers in order to obtain a total thickness ≤700 nm. Bi-layers were deposited using the deposition parameters supplied in table 5.2.

Table 5.2: Bi-layer deposition properties.

Bi-layer	Layers	T_s(°C)	p (*10^{-3}mbar)	p_{water}(*10^{-5}mbar)	t (s)	P (W)	d (nm)
2A	IOH	25	5,7	3	2000	150	558
	i-ZnO	200	2,6	-	3600	200	
11A	IOH	25	5,7	3	1100	150	594
	i-ZnO	200	2,6	-	5060	200	
12A	IOH	25	5,7	3	1100	150	586
	i-ZnO	200	2,6	-	4200	200	

5.2. DEPOSITION AND ANALYSIS

The first bi-layers were deposited successfully where strips of 2,5x10 cm were almost completely coated with IOH on top of which a mask was placed in order to partially coat the IOH with i-ZnO.

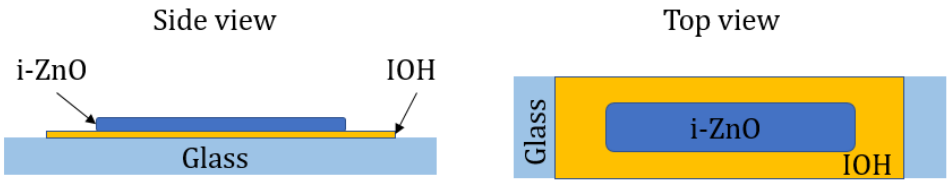

Figure 5.2: Schematic side view and top view of first bi-layers.

Figure 5.2 depicts a schematic overview of the bi-layers where a clear distinction could be made between the IOH and i-ZnO films due to the light reflecting off of the surfaces. Average thicknesses of +/- 580 nm were measured indicating that i-ZnO has moderate adhesion on to IOH coated glass. The decision for coating the IOH partially with i-ZnO was initially made just in case the i-ZnO would not adhere as well to IOH and for measurement reasons in case i-ZnO would retain its poor electrical properties. The following figures depict the optical properties for the as deposited bi-layers compared to the individual IOH and i-ZnO layer.

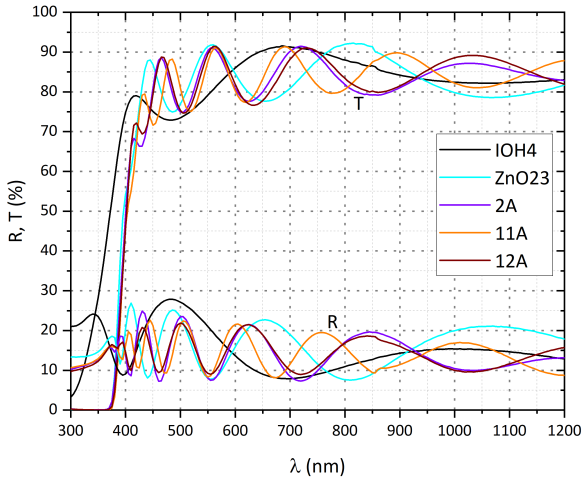

Figure 5.3: Reflectance and transmittance for the individual layers mentioned in table 5.1 compared to reflectance and transmittance for the bi-layers mentioned in table 5.2.

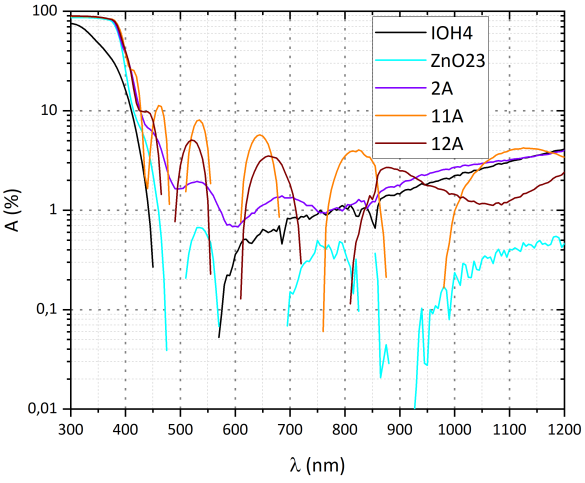

Figure 5.4: Absorbance for the individual layers mentioned in table 5.1 compared to absorbance for the bi-layers mentioned in table 5.2.

Table 5.3: Electrical properties individual layers compared to bi-layers.

Sample	N_e (*10^{20}/cm^3)	μ(cm^2/Vs)	ρ (*10^{-4} Ω*cm)
IOH4	11,10	21,50	2,60
ZnO23	-	-	-
2A	2,10	27,30	10,90
11A	0,70	34,50	26,60
12A	0,80	36,90	21,60

Due to their thickness, the reflectance and transmittance spectra of the bi-layers in figure 5.3 contain more interference patterns compared to the individual layers. Still they retain a similar high transparency and low reflectance over the broad wavelength range. When the NIR absorbance is considered in figure 5.4, it can be seen that the bi-layers all posses an absorbance ≥1%, in better agreement with the individual IOH layer than the i-ZnO layer. The bi-layers keep forming interference patterns up to the UV region, where a better agreement is reached with i-ZnO, seeing as they become almost completely absorbing between 300 nm and 400 nm. Table 5.3 displays the electrical properties measured for the as deposited bi-layers compared to the individual layers. In contrast to the highly resistive single ZnO23 layer, electrical properties for the bi-layers could be measured, pointing out that a electrical path through through IOH is possible. A lower carrier density is observed for bi-layer 2A which was deposited using the exact same deposition conditions as IOH4, while the mobility and resistivity are higher. These properties are possibly an effect of depositing i-ZnO on top, where some crystallisation of the IOH layer may take place during deposition resulting in a decrease in defect density. When a thinner IOH layer and thicker i-ZnO layer are deposited as bi-layers 11A and 12A, a stronger decrease in carrier density combined with an increase in carrier mobility and resistivity are observed. The columnar grain structure of i-ZnO contributes to a better transverse conductivity to IOH, while a thin IOH layer contributes to high lateral conductivity resulting in the mobilities observed in table 5.3. Judging from the individual IOH resistivity, the higher bi-layer resistivities seem to be caused by the path followed by carriers through i-ZnO.

5.3. IMPROVEMENT

The bi-layers appear to posses electrical properties close to or even slightly improved compared to those of an individual IOH layer. Moderate mobilities and carrier density's along with moderate absorbance and transmittance in the NIR point to a working front TCO for solar cells.

In an attempt for improvement, the previously displayed samples were subjected to ambient annealing at 215 °C for 20 minutes leading to significant improvement. Further exposure to ambient annealing for longer times lead to electrical properties far exceeding both individual IOH and i-ZnO. An annealing time of 80 minutes lead

to carrier mobilities >100 cm^2/Vs and carrier density's dropping to even lower than initial values.

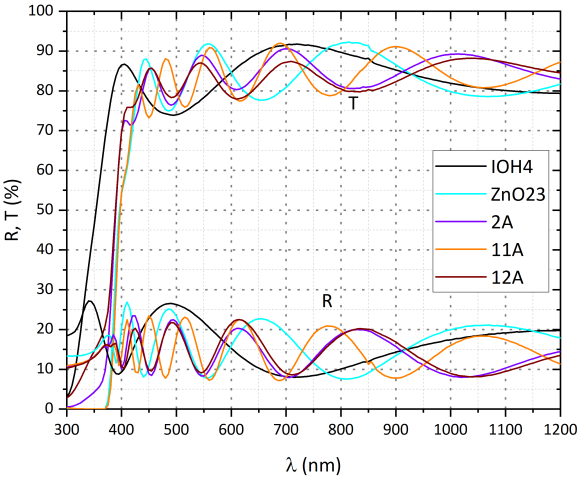

Figure 5.5: Reflectance and transmittance for the individual layers mentioned in table 5.1 compared to reflectance and transmittance for the bi-layers mentioned in table 5.2. IOH4 was annealed for 30 minutes and the bi-layers were annealed for 80 minutes at 215 °C in an ambient atmosphere.

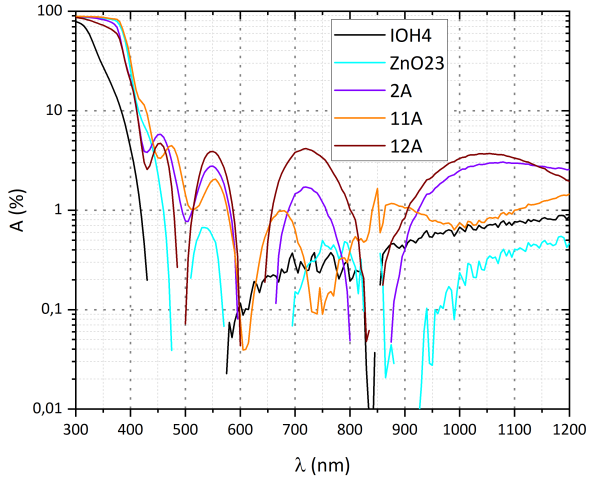

Figure 5.6: Absorbance for the individual layers mentioned in table 5.1 compared to absorbance for the bi-layers mentioned in table 5.2. IOH4 was annealed for 30 minutes and the bi-layers were annealed for 80 minutes at 215 °C in an ambient atmosphere.

Table 5.4: Electrical properties annealed bi-layers compared to annealed IOH layer.

Sample	N_e (*10^{20}/cm^3)	μ(cm^2/Vs)	ρ (*10^{-4} Ω*cm)
IOH4	3,00	71,60	2,90
ZnO23	-	-	-
2A	0,80	73,20	10,70
11A	0,30	97,90	22,00
12A	0,30	103,70	21,70

Transmittance and reflectance for the annealed bi-layers in figure 5.5 appear to follow a similar trend compared to the non annealed bi-layers in figure 5.3. NIR absorbance, however, has decreased for bi-layers 2A and 11A, while bi-layer 12A experiences a small increase in absorbance.

In terms of electrical properties, the bi-layers all exceed the single IOH layer, where bi-layer 2A has the closest mobility to IOH4. Samples 11A and 12A posses the highest mobilities achieved, surpassing the initial bi-layer architecture of sample 2A as well as IOH4 by an exceeding amount. The resistivities do not experience significant changes after annealing, due to the combined increase in mobility and decrease in carrier density.

5.4. INVESTIGATION

Initially, annealing IOH single layers at temperatures higher than 215 °C for long annealing times was thought to lead to hydrogen diffusing out of the sample, meaning a withdrawal of carriers initially present in the sample as a result of doping. The reason for enhancement due to annealing the bi-layers was first thought to be the result of i-ZnO acting as a capping layer on top of IOH in a way that hydrogen was being trapped in the IOH layer by i-ZnO.

As a means of investigating the diffusion of hydrogen out of the samples, individual IOH layers as well as bi-layers were exposed to temperatures in a range of 200 °C to 600 °C with 50 °C increments using a hydrogen desorption detecting setup (TDS) with holding times of 20 minutes in between. No hydrogen was detected escaping any of the layers, indicating that either the amount of hydrogen diffusing out of the samples is too small to be detected in the TDS environment or no hydrogen is diffusing out of the samples.

A second attempt was made to find an explanation by performing SEM cross sectional analysis on the as deposited and annealed samples. The interface between the two layers was thought to fade into a gradient by annealing. Figure 5.7 depicts the as deposited and annealed cross sections for bi-layer 11A.

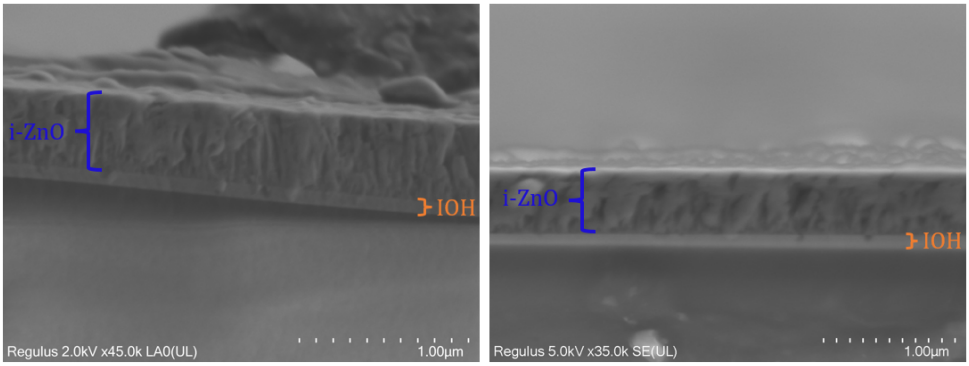

(a) (b)

Figure 5.7: (a) SEM cross section of sample 11A as deposited. (b) SEM cross section of sample 11A subjected to ambient atmosphere PDA at 215 °C for 80 minutes.

From figure 5.7 a clear distinction can be made between the two films before as well as after annealing, where the interface remained intact and no gradient is observed between the two films. The IOH film has a smooth surface on top of which ZnO grains are grown.

For the purpose of demonstrating the importance and effect of deposition order, sample 12A from table 5.2 was deposited in reverse i.e. i-ZnO on glass followed by IOH on top of i-ZnO. These reversed samples were observed to own similar optical

properties compared to the originals although, showed poor performance in terms of electrical properties. Mobilities no higher than 16 cm^2/Vs with carrier densities of $0{,}2*10^20$ $/cm^3$ were measured for as deposited samples. Ambient atmosphere annealing at 215 °C for 80 minutes (the same as for the original samples), resulting in detrimental effects on the electrical properties. Mobilities decreased to values between 10 cm^2/Vs and 6 cm^2/Vs, while retaining an as deposited carrier density. These mobilities and carrier densities lie between that of the single as deposited IOH and i-ZnO layer. The i-ZnO surface on top of which IOH is deposited has a higher roughness than flat corning glass, which may be the root of these properties.

Further investigation lead to XRD analysis on the as deposited and annealed bi-layers. The possibility of i-ZnO acting as a "post-seeding" layer improving the crystallinity of IOH upon annealing was theorised to have been the cause for improvement. The crystallinity of a single IOH layer was first investigated pre -and post annealing followed by an analysis of the pre -and post annealed bi-layer.

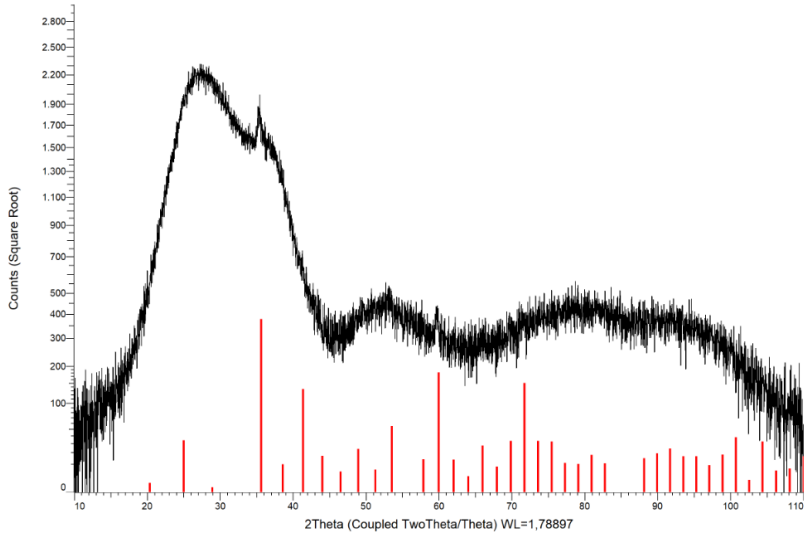

Figure 5.8: XRD spectrum of as deposited IOH4. Reference XRD spectrum of standard In_2O_3 shown as red bars on the horizontal axis.

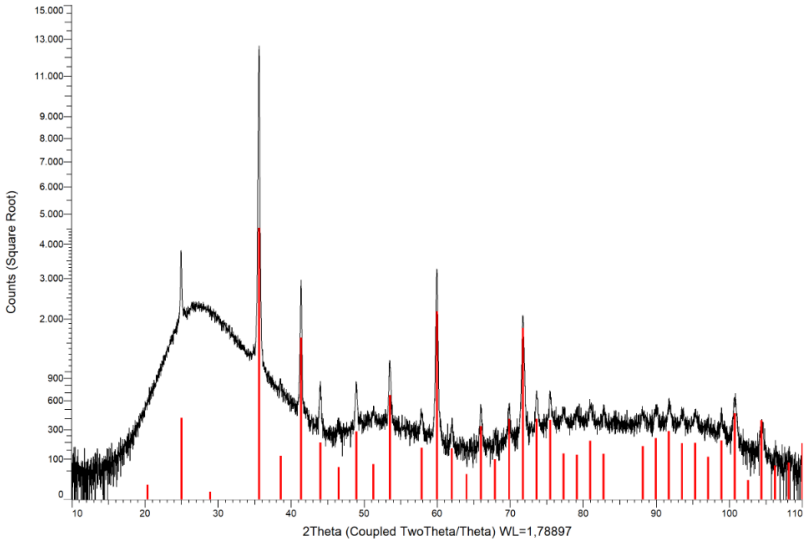

Figure 5.9: XRD spectrum of annealed IOH4, annealed at 215 °C for 60 minutes. Reference XRD spectrum of standard In_2O_3 shown as red bars on the horizontal axis.

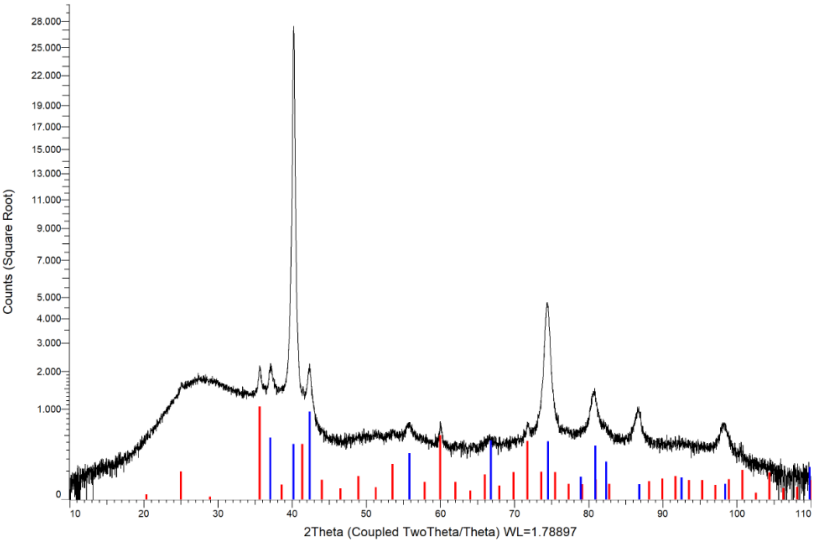

Figure 5.10: XRD spectrum of as deposited bi-layer 11A. Reference XRD spectrum of standard In_2O_3 and i-ZnO shown as red and blue bars respectively on the horizontal axis.

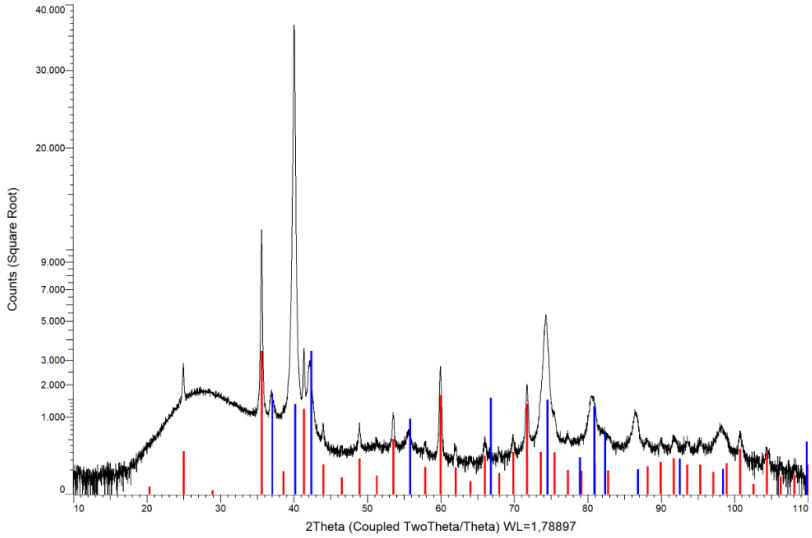

Figure 5.11: XRD spectrum of annealed bi-layer 11A, annealed at 215 °C for 80 minutes. Reference XRD spectrum of standard In_2O_3 and i-ZnO shown as red and blue bars respectively on the horizontal axis.

Initially, the as deposited single IOH4 layer as seen in figure 5.8 is completely amorphous. After annealing this sample, a strong transformation from amorphous to crystalline is observed as seen in figure 5.9. Average crystallinity of the samples was calculated by determining the peak area of the four strongest peaks present which were normalised by dividing by the theoretical relative intensities. After annealing, the crystallinity for IOH4 increased from 0,6% to 100% (±9%). The as deposited bi-layer 11A is observed to posses little crystallinity for its IOH layer compared to the single IOH layer, while the i-ZnO layer is crystalline upon deposition as depicted in figure 5.10. The sample possessed an overall average crystallinity of 27% (±6%). Figure 5.11 demonstrates the solid phase crystallisation for the bi-layer as a result of annealing the sample with the overall average crystallinity increasing to 88% (±9%). The intensity measured for IOH peaks in figure 5.11 is comparable to the intensity for the annealed single IOH4 in figure 5.9, pointing out that i-ZnO does not contribute to the crystallinity of IOH. The explanation of i-ZnO acting as a post seeding layer improving the crystallinity of IOH upon annealing was therefore disproved. The improved overall crystallinity is thought to be one of the most probable explanations for the superiority of the bi-layers.

6

CONCLUSION

This chapter has been divided into four sections: ITO, IOH, i-ZnO and Bi-layer. Each section will provide conclusive remarks concerning their respective titles.

ITO

Increasing T_s resulted in decrease of carriers in the film until 146 °C. This temperature counterintuitively resulted in higher NIR absorbance compared to films deposited at lower T_s due to the higher amount of charge carriers present in the film. Higher temperatures are known to result in better crystallisation however, temperatures were not sufficiently high for the films to crystallise, therefore they are reasoned to be (mostly) amorphous with little control over their electrical properties.

Deposition power has significant influence on film thickness. Too low of a deposition power transfers little kinetic energy to the target leading to a random orientation and grain growth. Increasing power up to the available maximum however is not the solution to obtaining the highest quality films. This limit on the power exists due to the sputtering damage inflicted upon a forming film by the increased amount of collisions within the plasma leading to a decrease in mobility.

Film thickness increased with increasing deposition time. A constant deposition rate can be determined by dividing the deposition time by film thickness, while all other deposition conditions are kept constant. Sample crystallinity may be increased with increasing deposition time, provided the temperature is sufficiently high in order to stimulate crystallisation. At room temperature however, the films are amorphous and and increasing time contributes to an increasing defect density illustrated by the increasing amount of carriers.

IOH

Doping In_2O_3 with hydrogen by introducing water vapour to the sputtering chamber lead to the formation of hydrogen doped indium oxide. Substrate temperature for

IOH has a similar effect on film quality compared to ITO. The extra variable of water vapour added during deposition suppresses lateral grain growth resulting in films which are highly amorphous. Increasing substrate temperature also results in an increasing crystallinity which is observed by the decrease in NIR absorption as well as decrease in carrier concentration. Increasing water vapour pressure only at room temperature depositions lead to IOH films experiencing higher amounts of doping however, the amorphous nature of the films due to the presence of water vapour remained present, attributed to the formation of hydroxyl groups in the growing doped In_2O_3 film.

As deposited IOH samples were observed to posses higher carrier densities and higher mobilities compared to ITO samples. As a means of improving IOH films, they were subjected to PDA in an ambient atmosphere within a temperature range of 100 °C to 300 °C, where an optimum annealing temperature of 215 °C resulted in a significant increase in mobility along with a decrease in carrier density. Annealing samples resulted in crystallisation where dangling bonds are passivated and diffusion lead to vacancies being filled. Annealing times longer than 20 minutes resulted in no significant improvement pointing out that the crystallisation has saturated at this annealing time. Films deposited at room temperature were found to respond better to annealing compared to films deposited at higher temperatures with respect to mobility and carrier density. Mobilities as high as 71,60 cm^2/Vs with carrier densities of $3*10^{20}/cm^3$ were observed for room temperature deposited films after annealing, while annealed films which were deposited at higher temperatures showed mobilities no higher than 50 cm^2/Vs with carrier densities of $1,5*10^{20}/cm^3$. Total crystallisation by annealing completely amorphous samples after deposition resulted in films with the most desired properties.

I-ZNO

Regardless of the deposition parameters, i-ZnO films are crystalline. In order to deposit i-ZnO films, higher substrate temperatures and RF powers were required compared to ITO and IOH. The intrinsic nature lead to lower carrier densities compared aforementioned TCO's leading to NIR absorption ≤1%. Electrical properties of i-ZnO were not consistently accurately measurable due to the microstructure formed lateral resistance along the path carriers follow.

BI-LAYER

In terms of electrical properties, IOH was demonstrated to have a clear advantage compared to ITO and i-ZnO, while the NIR absorbance of i-ZnO was the lowest of the three. A bi-layer composed of IOH and i-ZnO was constructed where the highest mobility IOH sample and the i-ZnO sample with lowest NIR absorbance were selected. As deposited bi-layers resulted in higher mobility and lower carrier density compared to as deposited IOH and i-ZnO layers. PDA of these samples lead to an improvement of the opto-electrical properties where the electrical properties

especially the mobility exceeded even that of annealed IOH. Further tinkering with deposition times lead to an even stronger improvement after PDA leading to the best bi-layer which consisted of a thin IOH layer followed by a thick i-ZnO layer. This sample had a mobility of 103,70 cm^2/Vs along with an NIR absorption fluctuating between 4% and values lower than 1%. Bi-layers consisting of a thin IOH and thick i-ZnO layer were thus successfully created with opto-electrical properties surpassing either individual film.

Amorphous IOH has been illustrated not experience enhanced crystallisation as a result of i-ZnO when the bi-layer was annealed. The effect of i-ZnO acting as a post seeding layer, resulting in the enhanced mobility has therefore been disproved. The layers have also been deposited in reversed order for the purpose of exploring the capping layer effect of i-ZnO. These samples, although deposited under the same conditions, resulted in mobilities no higher than 16 cm^2/Vs, pointing out the importance of deposition order.

The annealing effect resulted in significant improvement of the mobility in particular. SEM cross sectional analysis revealed that the interface between the two films did not fade into a gradient after annealing, but remained as is instead. The working theory is the capping effect which i-ZnO has on the IOH layer in a sense that it keeps hydrogen from diffusing out of the sample during annealing. The detrimental effects on the electrical properties of IOH when annealing at temperatures higher than 215 °C have been demonstrated in this paper and may be a result of hydrogen diffusing out of the film. When hydrogen is trapped in the bi-layer, it may diffuse within the film in order to accommodate defects when IOH crystallises during annealing. The capping layer theory was investigated using a hydrogen desorption detecting setup, but no hydrogen was detected diffusing out of the IOH as well as the bi-layers. This result could however mean that the setup applied for this investigation does not posses the sensitivity to detect the small amount of hydrogen escaping previously mentioned samples.

7

RECOMMENDATIONS

Hydrogen doping of In_2O_3 has a crucial effect on its opto-electrical properties, which is why further investigation on the behaviour of hydrogen within the deposited IOH and bi-layer is required. The amount of hydrogen present in deposited films along with the bonds formed can be detected using Fourier transform infrared spectroscopy. The effect of annealing on the hydrogen bonds within the samples should be a main focus point, as this will lead to a clarified understanding of the bi-layer superiority. With an i-ZnO layer on top of IOH, hydrogen may also be diffusing in to the i-ZnO films resulting in n-type ZnO.

Annealing proved to be a crucial step for increasing bi-layer mobility, thus increasing conductivity. In this report, samples were annealed in an ambient atmosphere using optimum annealing temperatures of 215 °C. Annealing atmosphere can influence the crystallisation as well as defect density within the film. A hydrogen environment may enhance mobility by diffusion of hydrogen to vacancies and allow stronger passivation of dangling bonds. Further more, if hydrogen diffuses out of the sample during ambient atmosphere annealing for the annealing times utilised in this report, shorter annealing times with higher temperatures may form a solution. Rapid thermal processing allows annealing at temperatures >400 °C for a manner of seconds, which may conserve the hydrogen within the sample.

Surface morphology of the as deposited as well as annealed TCO films should give a clear idea of the annealing effect on grain growth. Depositing i-ZnO on IOH as opposed to flat glass may result in better lateral grain growth for both i-ZnO as well as IOH after annealing, leading to the high electron mobilities presented in this paper. Atomic force microscopy is a surface characterisation technique recommended for analysing the surface morphology of the TCO's mentioned in this paper.

BIBLIOGRAPHY

[1] A. H. Smets, K. Jäger, O. Isabella, R. A. Swaaij, and M. Zeman. *Solar Energy: The physics and engineering of photovoltaic conversion, technologies and systems*. UIT Cambridge, 2015.

[2] E. D. Coyle and R. A. Simmons. *Understanding the global energy crisis*. Purdue University Press, 2014.

[3] N. US Department of Commerce. *Global Monitoring Laboratory - Carbon Cycle Greenhouse Gases*. URL: https://gml.noaa.gov/ccgg/trends/.

[4] T. D. Lee and A. U. Ebong. "A review of thin film solar cell technologies and challenges". In: *Renewable and Sustainable Energy Reviews* 70 (2017), pp. 1286–1297.

[5] F. Saitta. "Flexible, lightweight, silicon-based triple junction solar cell development". In: (2021).

[6] G. R. Fowles. *Introduction to modern optics*. Courier Corporation, 1989.

[7] M. stage transistor amplifiers Chapter. "ECE255 Electronic Circuit Analysis and Design". In: *signal* 1 (2013), p. 8.

[8] A. Sproul. "Understanding the pn Junction". In: *Solar Cells: Resource for the Secondary Science Teacher* 73 (2003).

[9] Y. Kindaichi. *Energy Band of pn junction in thermal equilibrium (Zero bias)*. Mar. 2020. URL: https://physics.stackexchange.com/questions/537166/energy-band-of-pn-junction-in-thermal-equilibrium-zero-bias.

[10] A. Cultrera, C. Lamberti, and L. Boarino. "Effects of adsorbates on the electrical and optical properties of mesoporous semiconductors". In: *no. June* (2014).

[11] C. Han. "High-Mobility TCO-Based Contacting Schemes for c-Si Solar Cells". In: (2022).

[12] A. Varanasi. "Deposition of hydrogen-doped indium oxide thin films using atmospheric-pressure plasma-enhanced spatial atomic layer deposition". In: (2017).

[13] P. Babál. "Doped nanocrystalline silicon oxide for use as (intermediate) reflecting layers in thin-film silicon solar cells". In: (2014).

[14] F. Shi. *Introductory Chapter: Basic Theory of Magnetron Sputtering [Online First]. Rijeka: IntechOpen; 2018. DOI: 10.5772/intechopen. 80550.*

[15] M. Ohring. *Materials Science of Thin Films: Depositon and Structure*. Elsevier, 2001.

[16] Designua. *Visible spectroscopy. Spectrophotometry. molecular analysis using UV stock vector - illustration of emissions, chemistry: 205382843*. Dec. 2020. URL: https://www.dreamstime.com/visible-spectroscopy-spectrophotometry-molecular-analysis-using-uv-visible-spectroscopy-spectrophotometry-molecular-analysis-using-image205382843.

[17] *Perkin Elmer, Applications and Use of Integrating Spheres With the LAMBDA 650 and 850 UV/Vis and LAMBDA 950 UV/Vis/NIR Spectrophotometers, (2004)*. URL: https://resources.perkinelmer.com/corporate/cmsresources/images/44-74191app_lambda650integratingspheres.pdf.

[18] *Spectroscopic Ellipsometry: Basic Concepts*. URL: https://www.horiba.com/int/scientific/technologies/spectroscopic-ellipsometry%20/spectroscopic-ellipsometry/.

[19] J.-H. Kang, S.-H. Lee, H. Ruh, and K.-M. Yu. "Development of a thickness meter for conductive thin films using four-point probe method". In: *Journal of Electrical Engineering & Technology* 16.4 (2021), pp. 2265–2273.

[20] *WHAT IS X-RAY DIFFRACTION ANALYSIS (XRD) AND HOW DOES IT WORK?* URL: https://www.twi-global.com/technical-knowledge/faqs/x-ray-diffraction#:~:text=X%2Dray%20diffraction%20analysis%20(XRD)%20is%20a%20technique%20used,leave%20the%20material%20%5B1%5D..

[21] *Bradbury, S. , Ford, . Brian J. and Joy, . David C. (2023, February 15). scanning electron microscope. Encyclopedia Britannica*. URL: https://www.britannica.com/technology/scanning-electron-microscope.

[22] G. M. Crankovic. *ASM Handbook, Volume 10:.: Materials Characterization*. ASM International, 1986.

[23] O. Bierwagen. "Indium oxide—a transparent, wide-band gap semiconductor for (opto) electronic applications". In: *Semiconductor Science and Technology* 30.2 (2015), p. 024001.

[24] S. Limpijumnong, P. Reunchan, A. Janotti, and C. G. Van de Walle. "Hydrogen doping in indium oxide: An ab initio study". In: *Physical Review B* 80.19 (2009), p. 193202.

[25] C. Yuan, X. Liu, C. Ge, W. Li, K. Li, L. Fu, X. Zeng, H. Song, Y. He, X. Xiao, *et al.* "Stable Indium Tin Oxide with High Mobility". In: *ACS Applied Materials & Interfaces* 14.44 (2022), pp. 49937–49944.

[26] Ç. Kılıç and A. Zunger. "Origins of coexistence of conductivity and transparency in SnO 2". In: *Physical review letters* 88.9 (2002), p. 095501.

[27] F. Kurdesau, G. Khripunov, A. Da Cunha, M. Kaelin, and A. Tiwari. "Comparative study of ITO layers deposited by DC and RF magnetron sputtering at room temperature". In: *Journal of non-crystalline solids* 352.9-20 (2006), pp. 1466–1470.

[28] A. P. Amalathas and M. M. Alkaisi. “Effects of film thickness and sputtering power on properties of ITO thin films deposited by RF magnetron sputtering without oxygen”. In: *Journal of Materials Science: Materials in Electronics* 27 (2016), pp. 11064–11071.

[29] S. Ishibashi, Y. Higuchi, Y. Ota, and K. Nakamura. “Low resistivity indium–tin oxide transparent conductive films. II. Effect of sputtering voltage on electrical property of films”. In: *Journal of Vacuum Science & Technology A: Vacuum, Surfaces, and Films* 8.3 (1990), pp. 1403–1406.

[30] A. Hacini, A. H. Ali, and N. N. Adnan. “Optimization of ITO thin film properties as a function of deposition time using the swanepoel method”. In: *Optical Materials* 120 (2021), p. 111411.

[31] L. Kerkache, A. Layadi, E. Dogheche, and D. Remiens. “Physical properties of RF sputtered ITO thin films and annealing effect”. In: *Journal of Physics D: Applied Physics* 39.1 (2005), p. 184.

[32] A. Tchenka, A. Agdad, M. C. Samba Vall, S. K. Hnawi, A. Narjis, L. Nkhaili, E. Ibnouelghazi, and E. Ech-Chamikh. “Effect of RF sputtering power and deposition time on optical and electrical properties of indium tin oxide thin film”. In: *Advances in Materials Science and Engineering* 2021 (2021), pp. 1–14.

[33] S. Li, Z. Shi, Z. Tang, and X. Li. “Study on the hydrogen doped indium oxide for silicon heterojunction solar cell application”. In: *Journal of alloys and compounds* 705 (2017), pp. 198–204.

[34] T. Koida, H. Fujiwara, and M. Kondo. “Hydrogen-doped In2O3 as high-mobility transparent conductive oxide”. In: *Japanese journal of applied physics* 46.7L (2007), p. L685.

[35] T. Koida, H. Fujiwara, and M. Kondo. “Structural and electrical properties of hydrogen-doped In2O3 films fabricated by solid-phase crystallization”. In: *Journal of Non-Crystalline Solids* 354.19-25 (2008), pp. 2805–2808.

[36] R. Muydinov, A. Steigert, M. Wollgarten, P. P. Michałowski, U. Bloeck, A. Pflug, D. Erfurt, R. Klenk, S. Körner, I. Lauermann, *et al.* “Crystallisation phenomena of In2O3: H films”. In: *Materials* 12.2 (2019), p. 266.

[37] S. C. Dixon, D. O. Scanlon, C. J. Carmalt, and I. P. Parkin. “n-Type doped transparent conducting binary oxides: an overview”. In: *Journal of Materials Chemistry C* 4.29 (2016), pp. 6946–6961.

[38] M. Boccard, N. Rodkey, and Z. C. Holman. “Properties of hydrogenated indium oxide prepared by reactive sputtering with hydrogen gas”. In: *2016 IEEE 43rd Photovoltaic Specialists Conference (PVSC)*. IEEE. 2016, pp. 2868–2870.

[39] S. Hussain. *Investigation of structural and optical properties of nanocrystalline ZnO*. 2008.

[40] O. Martınez, J. Plaza, J. Mass, B. Capote, E. Diéguez, and J. Jiménez. “Luminescence of pure and doped ZnO films synthesised by thermal annealing on GaSb single crystals”. In: *Superlattices and Microstructures* 42.1-6 (2007), pp. 145–151.

[41] K. U. Sim, S. W. Shin, A. Moholkar, J. H. Yun, J. H. Moon, and J. H. Kim. “Effects of dopant (Al, Ga, and In) on the characteristics of ZnO thin films prepared by RF magnetron sputtering system”. In: *Current Applied Physics* 10.3 (2010), S463–S467.

[42] J. Kennedy, P. Murmu, J. Leveneur, A. Markwitz, and J. Futter. “Controlling preferred orientation and electrical conductivity of zinc oxide thin films by post growth annealing treatment”. In: *Applied Surface Science* 367 (2016), pp. 52–58.

[43] Ü. Özgür, Y. I. Alivov, C. Liu, A. Teke, M. Reshchikov, S. Doğan, V. Avrutin, S.-J. Cho, Morkoç, and H. “A comprehensive review of ZnO materials and devices”. In: *Journal of applied physics* 98.4 (2005), p. 11.

[44] Y.-M. Lu, W.-S. Hwang, W. Liu, and J. Yang. “Effect of RF power on optical and electrical properties of ZnO thin film by magnetron sputtering”. In: *Materials chemistry and physics* 72.2 (2001), pp. 269–272.